Carbohydrate Polymers 324 (2024) 121423

Contents lists available at ScienceDirect

Carbohydrate Polymers

journal homepage: www.elsevier.com/locate/carbpol

Structural elucidation of a highly branched α-D-glucan from Huangjiu and its hepatoprotective activity via gut microbiome regulation and intestinal barrier repairment

Yi Yang [a], Qingxi Ren [a,b,c], Zhilei Zhou [a,b,c], Xiong Li [d], Dongliang Ren [a], Zhongwei Ji [a,b,c], Jian Mao [a,b,c,e,*]

[a] National Engineering Research Center of Cereal Fermentation and Food Biomanufacturing, School of Food Science and Technology, Jiangnan University, Wuxi 214122, Jiangsu, China
[b] Jiangnan University (Shaoxing) Industrial Technology Research Institute, Shaoxing 312000, Zhejiang, China
[c] Jiangsu Provincial Engineering Research Center for Bioactive Product Processing, Jiangnan University, Wuxi 214122, Jiangsu, China
[d] Southern Marine Science and Engineering Guangdong Laboratory (Guangzhou), 1119 Haibin Road, Guangzhou 511458, Guangdong, China
[e] National Engineering Research Center for Huangjiu, Zhejiang Guyuelongshan Shaoxing Wine Co., Ltd, Zhejiang Shaoxing Huangjiu Industry Innovation Service Complex, Shaoxing, Zhejiang 312000, China

ARTICLE INFO

Keywords:
Huangjiu polysaccharide
Nuclear magnetic resonance spectroscopy
Alcoholic liver damage
Gut microbiota
Intestinal barrier function
Short-chain fatty acids

ABSTRACT

Polysaccharides in Huangjiu, a traditional fermented food, are expected to be potentially effective ingredients in protecting against alcoholic liver disease (ALD). Elucidating their precise structural and functional characteristics is essential for in-depth understanding of structure-activity relationships of hepatoprotective polysaccharides. Herein, a major polysaccharide component HJPS1–2 was purified from Huangjiu with an average molecular weight of 3.49 kDa. Structural analyses inferred that HJPS1–2 backbone was composed of (1 → 4)-linked α-D-Glcp and a single α(1 → 6)-D-Glcp-α(1 → 6)-D-Glcp branched unit for every three α(1 → 4)-D-Glcp. An ALD mouse model was further established to clarify the underlying effect of HJPS1–2 on ALD alleviation. Biochemical detection and histopathological assessment revealed that HJPS1–2 intervention remarkably improved ethanol-induced hepatic dysfunction and steatosis. HJPS1–2 treatment ameliorated gut microbiota dysbiosis of ALD mice in a dose-dependent manner, mainly manifested as restoration of microbial diversities, community structure and bacterial interaction patterns. Compared with ethanol group, the strikingly elevated intestinal short-chain fatty acids' levels and enhanced intestinal barrier function after HJPS1–2 intake might contribute to reduced serum and liver lipopolysaccharide levels and subsequently suppressed release of hepatic inflammatory cytokines, thus mitigating ALD. Collectively, this research supports the potential of food-derived polysaccharides to hinder the early formation and progression of ALD through maintaining intestinal homeostasis.

1. Introduction

Alcohol consumption is widely prevalent currently due to its unique social and cultural attributes. However, long-term alcohol abuse can lead to alcoholic liver disease (ALD), a progressive disease that may gradually develop from hepatic steatosis to cirrhosis and even liver cancer (Li et al., 2021). It is regarded as the primary cause of morbidity and mortality worldwide, and therefore becomes one of the public health issues of global concern (Ji, Fang, Jia, Du, & Xu, 2021). On account of the limited pharmacologic options for ALD treatment, exploring effective early intervention strategies to hinder the formation or delay the deterioration of ALD has become extremely momentous and urgent.

Essential contributions of gut microbial community to the host physiology and pathological disorders have been well documented (Addolorato et al., 2020; Guarner & Malagelada, 2003; Liu et al., 2021). However, ethanol (EtOH) exposure can not only directly perturb intestinal microbiota composition, but also indirectly arouse gut dysbiosis by altering the nutritional sources of microbes, such as diminishing all amino acids and branched chain amino acids in the intestine (Fan et al., 2019; Liu et al., 2020). Importantly, the generation of microbial

* Corresponding author at: National Engineering Research Center of Cereal Fermentation and Food Biomanufacturing, Jiangnan University, Wuxi 214122, Jiangsu, China.
E-mail address: maojian@jiangnan.edu.cn (J. Mao).

https://doi.org/10.1016/j.carbpol.2023.121423
Received 3 July 2023; Received in revised form 14 September 2023; Accepted 19 September 2023
Available online 21 September 2023

metabolites associated with pathogen-associated molecular patterns (PAMPs) leads to the increment of intestinal permeability and bacterial translocation, which in turn induces systemic inflammation (Fang et al., 2019). Recent studies increasingly highlighted the crucial influence of gut-liver axis abnormalities resulted from gut microbiome imbalance on ALD pathophysiology (Liu, Zhao, Yang, & Zhao, 2019; Sarin, Pande, & Schnabl, 2019). Furthermore, modulation of gut microbiota composition via fecal microbiota transfer, oral probiotics therapy or prebiotics supplementation has been confirmed to be effective in improving ALD (Li et al., 2021; Sarin et al., 2019; Teng et al., 2023).

It is well established that polysaccharides are natural products with a broad spectrum of biological effects, in which their application prospect in preventing ALD has drawn extensive attention (Teng et al., 2023; Yang et al., 2020). Of note, hepatoprotective polysaccharides displayed diverse merits of non-toxic or low side effect, multi-pathway and multi-target, thus having the potential to be developed as complementary or alternative therapies for liver protection agents (Cao, Lv, Zhang, & Chen, 2019; Yang et al., 2020; Zhang et al., 2016). Fermented foods are progressively favored for their attractive economic and nutritional value, which prompts more in-depth exploration of food fermentation. The fermentation process is expected to become a potential and promising approach for the treatment and structural modification of polysaccharides, in order to enhance their specific bioactivity and application diversification (Zhang et al., 2018). Recent researches supported the potent antioxidant, anti-inflammatory, hypoglycemic, anti-aging, anti-allergic, anti-tumor and immunomodulatory effects of functional polysaccharides derived from fermented foods (Kim, Lee, & Shin, 2016; Son, Kim, Park, & Shin, 2022; Yang, Hua, & Wang, 2019). For example, polysaccharide MWP isolated from *Malus micromalus Makino* fruit wine exhibited anti-aging effect, which was embodied in elevated activity of antioxidant enzyme system, remarkably restrained apoptosis of cerebral cortex cells and suppressed formation of lipid peroxide in an aging model after MWP intervention (Yang et al., 2019). The polysaccharide KBV-CP from Korean brown rice vinegar was identified to possess multiple intestinal immunostimulatory activities (Kim et al., 2016). Moreover, polysaccharide BF-I extracted from fermented barley presented efficacious tumor metastasis-suppressive activity in connection with diverse immune factors (Son et al., 2022).

Huangjiu, a typical grain-fermented low-alcoholic beverage (generally 14 %vol), is acknowledged as one of the three ancient wines worldwide, along with beer and grape wine. As a crucial constituent of traditional fermented foods, Huangjiu is renowned for its desirable flavor, subtle taste, plentiful nutrients and abundant functional ingredients, with a history of brewing and consumption for over 5000 years (Yang et al., 2022). It is basically brewed with cereal (for example, glutinous rice, foxtail millet and broomcorn millet) as raw material, wheat Qu as saccharification agent, and yeast as starter culture (Wang et al., 2022; Ye, Wang, Zhan, Tian, & Liu, 2022). The multitudinous bioactive substances in Huangjiu are inseparable from the complex microbial metabolism in the fermentation system, the distinctive bilateral fermentation process, as well as the low-temperature and long-term fermentation features (Chen et al., 2021). Interestingly, the partial antagonistic effect of non-alcoholic components (NAC) in Huangjiu on alcoholic hepatotoxicity was affirmed in our previous study (Yang et al., 2022). Polysaccharides are one of the most critical bioactive components in Huangjiu, mainly derived from the dissolution and enzymatic hydrolysis of polysaccharides in raw materials, as well as the secretion and metabolism of microorganisms (Chen et al., 2021; Peng, Liu, Ji, Chen, & Mao, 2019). Incremental evidence revealed various bioactivities of Huangjiu polysaccharides (HJPS), including antioxidant, antitumor, immune enhancement and anti-inflammatory effects (Peng et al., 2019; Shen, Mao, Chen, Meng, & Ji, 2015). Nevertheless, the precise structure information of HJPS has rarely been elucidated. Whether HJPS could confer protective effect against ALD, the relationship between dose and effect, and the possible hepatoprotective mechanisms remain unclear.

Herewith, the main polysaccharide fraction HJPS1–2 was isolated and purified from Huangjiu in the current study. Its structure was characterized by analyses of monosaccharide composition, methylation and nuclear magnetic resonance (NMR). Subsequently, an ALD mouse model was constructed to assess the alleviative influence of HJPS1–2 on ALD and investigate the potential associations between key differential operational taxonomic units (OTUs) and ALD-related host indicators via biochemical indexes determination, intestinal barrier function detection, gut microbiota profile analysis and intestinal short-chain fatty acids (SCFAs) quantification. Furthermore, it was speculated that enhancing the functionality of NAC to mitigate the probable health impairment of fermented alcoholic beverages warrants further exploration. Our findings might raise consumer awareness of specific dietary ingredients and provide a new perspective for early prevention and intervention of ALD.

2. Materials and methods

2.1. Materials and reagents

The raw material of Huangjiu without caramel color was provided by a local winery (Zhejiang Province, China). DEAE Sepharose Fast Flow and Sephadex G-50 were purchased from Beijing Solarbio Science & Technology Co., Ltd. (Beijing, China). Dextran standards, monosaccharide standards, silymarin, acetic acid, propionic acid, isobutyric acid, butyric acid, isovaleric acid, valeric acid and hexanoic acid were obtained from Sigma-Aldrich Co. (St. Louis, MO, USA). Lieber-DeCarli liquid diet was supplied by TROPHIC Animal Feed High-tech Co., Ltd. (Jiangsu, China). The commercial kits, including triglyceride (TG), total cholesterol (TC), aspartate aminotransferase (AST) and alanine aminotransferase (ALT) were acquired from Applygen Technologies Inc. (Beijing, China). Test kits for tumor necrosis factor-α (TNF-α), interleukin-1β (IL-1β), interleukin-6 (IL-6), lipopolysaccharide (LPS) and BCA were purchased from Thermo Fisher Scientific Inc. (Sunnyvale, CA, USA). Trizol reagent was gained from Beijing Kangwei Century Biotechnology Co., Ltd. (Beijing, China). PrimeScript™ RT Master Mix Kit and TB Green® Premix Ex Taq™ II kit were acquired from TaKaRa Bioengineering Inc. (Beijing, China). Fast DNA Spin Kit for Feces was provided by MP Biomedicals (Santa Ana, CA, USA). All primary and secondary antibodies were obtained from Servicebio (Wuhan, China). All other reagents used were of analytical grade and were supplied by Sinopharm Chemical Reagent Beijing Co., Ltd. (Beijing, China).

2.2. Isolation and purification of HJPS

Polysaccharides were extracted from Huangjiu following the method reported by Shen et al. (2015) with some modifications. Briefly, Huangjiu filtered by 0.22 μm membrane (Shaoxing Haina Membrane Technology Co., Ltd., Shaoxing, China) was concentrated by a R-1020 rotary evaporator (Hangzhou Gengyu Instrument Co., Ltd., Hangzhou, China) under reduced pressure at 55 °C with a concentration ratio of 10: 1. The concentrate was then precipitated twice to a final concentration of 90 % by adding anhydrous ethanol, stirred adequately and subsided at 4 °C for 24 h. The resulting precipitate from centrifugation (6000 ×*g*, 10 min) was dissolved with 30 % ethanol (*v/v*), stirred thoroughly, kept at 4 °C for 24 h and centrifuged (Himac CR21N, Tokyo, Japan) at 6000 × *g* for 10 min. Thereafter, the obtained supernatant underwent concentration and deproteinization by Sevage reaction (chloroform/n-butanol, 4: 1, *v/v*), followed by another concentration to remove the organic reagents. The resulting concentrate was ultrafiltered using a 3000 Da polyethersulfone membrane to remove the reducing sugars and oligosaccharides, and lyophilized to afford crude HJPS.

HJPS purification was carried out as previously reported with minor modifications (Teng et al., 2023). In brief, HJPS solution (10 mg/mL) was loaded on a pre-equilibrated DEAE Sepharose Fast Flow ion exchange column (15 mm × 800 mm) for stepwise elution with 0 M, 0.1 M,

0.2 M and 0.3 M NaCl solutions at a flow rate of 1.0 mL/min. The eluate was collected automatically at a rate of 6 mL/tube and monitored by phenol-H_2SO_4 colorimetric assay. Subsequently, four polysaccharide fractions were collected, merged and freeze-dried, namely, HJPS1, HJPS2, HJPS3 and HJPS4 (Fig. 1A). As the main component, HJPS1 solution (5 mg/mL) was further loaded a Sephadex G-50 gel column (15 mm × 800 mm) and eluted with distilled water at a flow rate of 0.3 mL/min (10 mL/tube). Another four fractions designated as HJPS1–1, HJPS1–2, HJPS1–3 and HJPS1–4, were acquired, pooled and lyophilized as described above. Finally, the major fraction HJPS1–2 was prepared for follow-up experiments.

2.3. Structural elucidation of HJPS1–2

2.3.1. Homogeneity and molecular weight (Mw) detection

The Mw determination was performed through a high-performance gel filtration chromatography (HPGFC) using a Waters 2695 HPLC system (Waters Corporation, MA, USA) equipped with a Waters 2414 refractive index detector, a TSKgel guard column (40 mm × 6.0 mm I.D., 12 μm) in series with a TSKgel $GMPW_{XL}$ column (300 mm × 7.8 mm I.D., 13 μm), and an Empower workstation. A 3 mg/mL sample was filtered through a 0.45 μm hydrophilic filter, injected into the HPGFC system with an injection volume of 10 μL, and then eluted with 0.1 M $NaNO_3$ solution at a flow rate of 0.5 mL/min. Dextran standards of T-2000 (2.00×10^6), T-300 (3.00×10^5), T-150 (1.35×10^5), T-10 (9.75×10^3) and T-5 (2.70×10^3) were used to establish a standard curve for Mw calculation.

2.3.2. Monosaccharide composition determination

Detection was conducted in high-performance anion exchange chromatography (HPAEC) based on a Dionex™ ICS-5000 system (Thermo, MA, USA), coupled with PAD, equipped with a CarboPac™ PA20 analytical column (3.0 mm × 150 mm) and a CarboPac™ PA20 guard column (3 mm × 50 mm). Concisely, a 5 mg sample was hydrolyzed with 2.0 mL of 2.0 M TFA under N_2 atmosphere at 120 °C for 3 h, then cooled to room temperature (25 °C). Next, 200 μL of methanol was added into the hydrolysate and the mixture was dried under N_2 blowing to remove the TFA (three times). Then, the dry reactant was dissolved in 10 mL of ultrapure water, filtered through a 0.22 μm organic filter, and analyzed by HPAEC. The mobile phase composed of ultrapure water (A), 1 M NaAc (B) and 250 mM NaOH (C) was set at a flow rate of 0.5 mL/min. The test column temperature was set at 30 °C and the injection

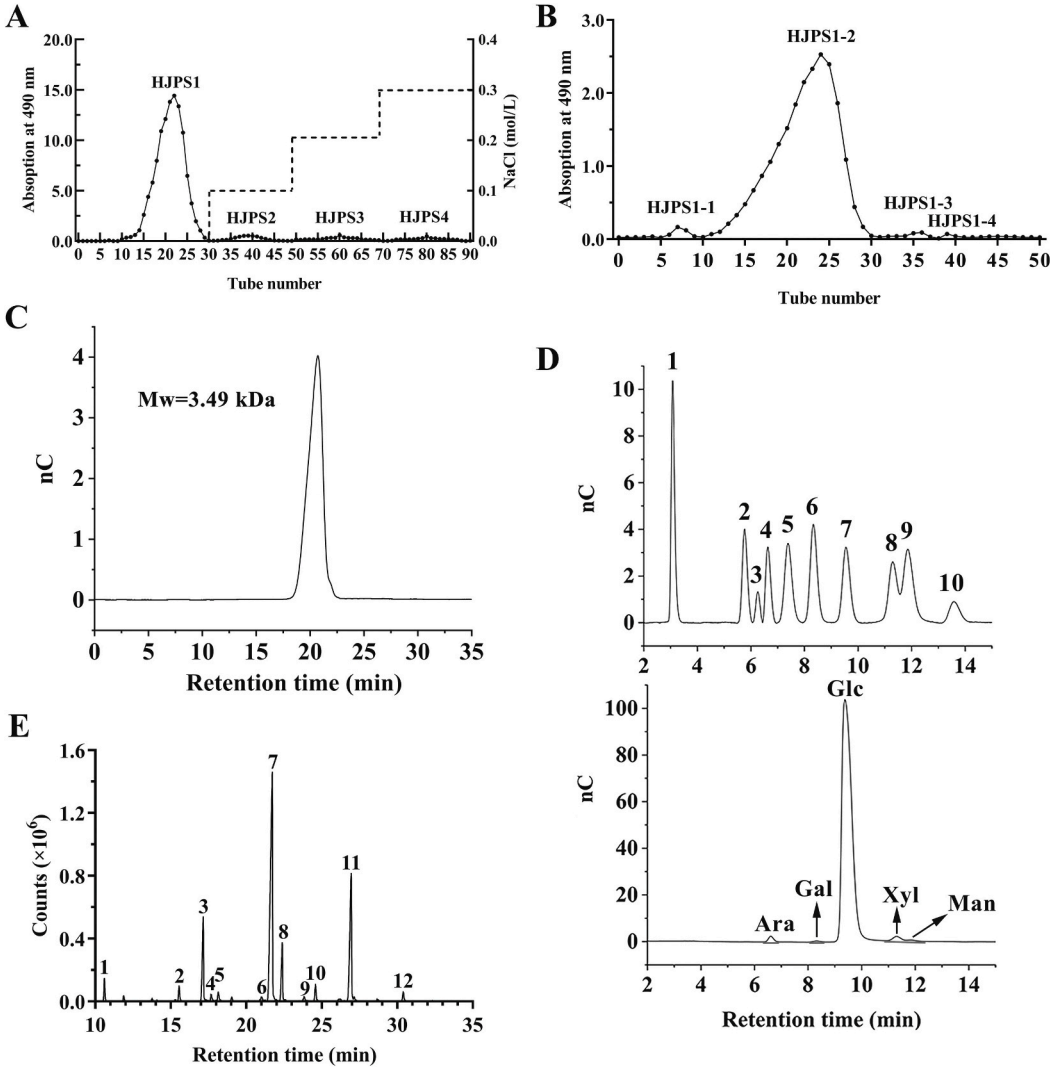

Fig. 1. Purification and physicochemical analysis of HJPS1–2. (A) The elution profile of HJPS on a DEAE Sepharose Fast Flow ion exchange column; (B) The elution curve of HJPS1 on a Sephadex G-50 gel column; (C) HPGFC chromatogram of HJPS1–2; (D) HPAEC-PAD chromatograms of mixed neutral monosaccharides' standards (upper) and hydrolysis products of HJPS1–2 (down). Peak identity: 1. fucose (Fuc), 2. galactosamine (GalN), 3. rhamnose (Rha), 4. arabinose (Ara), 5. glucosamine (GlcN), 6. galactose (Gal), 7. glucose (Glc), 8. xylose (Xyl), 9. mannose (Man), 10. fructose (Fru); (E) Total ion chromatogram of HJPS1–2 on GC–MS after methylation reaction.

volume was 20 μL.

2.3.3. Methylation examination

To explore glycosylic linkages, methylation analysis was carried out in an absolute desiccative environment as described previously (Wei et al., 2016) with slight modifications. In brief, 2–3 mg samples were mixed with 1 mL of DMSO and 20 mg of exsiccated NaOH, completely dissolved under sonication, and per-*O*-methylated with 1.5 mL of CH_3I in a water bath at 30 °C for 1 h under continuous magnetic stirring. The reaction was terminated with 2 mL of ultrapure water and the above methylation steps were repeated until the -OH bands of methylated samples were eliminated in the FTIR spectrums. Next, the reaction mixture was hydrolyzed with 1 mL of 2 M TFA at 110 °C for 2 h, reduced using 60 mg $NaBH_4$ for 8 h, acetylated with 1 mL of acetic anhydride at 100 °C for 1 h, isolated and desiccated as partially methylated alditol acetates (PMAAs) for GC–MS analysis (Shimadzu GCMS-QP 2010, Shimadzu Inc., Tokyo, Japan). The RXI-5 SIL MS capillary column (30 m × 0.25 mm id., 0.25 μm film thickness) used for PMAAs separation was programmed at 3 °C/min from 120 °C to 250 °C and kept at 250 °C for 5 min.

Qualitative authentication of PMAA derivatives was based on their retention times and representative electron-impact mass spectra (EI-MS), which were interpreted by referencing to the Complex Carbohydrate Research Center (CCRC) Spectral Database for PMAA's (https://glygen.ccrc.uga.edu/ccrc/specdb/ms/pmaa/pframe.html), standard database of Bo Rui Saccharide Biotech Co., Ltd. (Yang Zhou, Jiang Su, China) and published literatures (Li et al., 2020; Sassaki, Gorin, Souza, Czelusniak, & Iacomini, 2005; Xie et al., 2020; Zhang et al., 2021). Besides, relative molar ratios of different glycosyl linkages were calculated according to peak areas and response factors of PMAAs, as previously reported by Björndal, Lindberg, and Svensson (1967).

2.3.4. NMR spectrum analysis

Samples (35 mg) were first deuterium-exchanged for three times and then dissolved in 0.5 mL D_2O for NMR determination. NMR spectra were recorded on a Bruker™ Advance III spectrometer operating at 400 MHz (Bruker, Rheinstetten, Germany). The attribution of NMR signals was based on data from 1D NMR spectra (^1H, ^{13}C and DEPT-135), 2D NMR spectra (COSY, HSQC, HMBC, NOESY, and TOCSY) and literatures.

2.4. Hepatoprotective effect evaluation

2.4.1. Animals and treatments

Eight-week-old male specific-pathogen-free (SPF) C57BL/6J mice (weighing 25 ± 2 g) were purchased from Zhejiang Vital River Laboratory Animal Technology Co., Ltd. (Zhejiang, China) (SPF, SCXK (Zhe) 2019-0001). The mice were housed three or four per cage in a temperature and humidity-controlled environment and subjected to a 12-h light-dark cycle with ad libitum access to a chow diet and sterile water. The mouse model of chronic and binge ethanol feeding (the NIAAA model) was adopted in this research (Bertola, Mathews, Ki, Wang, & Gao, 2013). After a one-week acclimation period to the control liquid diet, the mice were randomly assigned to five groups (n = 10 each) as follows: (I) Control group (Ctrl); (II) ethanol group (EtOH); (III) positive control group (PC) fed 100 mg/kg bw silymarin; (IV) low-dose HJPS group (HJPS-L) received 400 mg/kg bw HJPS1–2; (V) high-dose HJPS group (HJPS-H) received 800 mg/kg bw HJPS1–2. Mice were pair-fed the Lieber-DeCarli liquid diet according to the experimental guidelines. Alcohol content of diets in EtOH, PC, HJPS-L and HJPS-H groups was gradually increased from 1 % to 5 % (*v/v*) and maintained at 5 % (*v/v*) for 10 days. On Day 11, mice were administered with a single dose of ethanol (5 g/kg bw) or isocaloric maltose dextrin by gavage in the early morning and euthanized 9 h later. Separated serum from centrifugation and quickly collected colonic contents were stored at −80 °C. A fraction of ileum and colon tissues were fixed in 4 % (*w/v*) paraformaldehyde solution and the rest was frozen at −80 °C. The entire liver was isolated and weighed, then fixed in 4 % (*w/v*) paraformaldehyde solution or cryopreserved at −80 °C. All the animal experimental procedures were approved by the Animal Ethics Committee of Jiangnan University (SPF, SYXK (Jiangsu) 2022-0053) (approval No: JN. No20210915c1401120[325]). A treatment schedule of this animal experiment is outlined in Fig. 4A.

2.4.2. Histopathological and immunofluorescence examinations

After 24 h of fixation, the liver, ileum and colon tissues were dehydrated in EtOH solutions, then embedded in paraffin, sliced into 4 μm sections, and stained with hematoxylin-eosin (H&E) for pathological observation. Additionally, the fixed liver samples were used for Oil Red O staining and the ileum slices were conducted the immunofluorescence assessment of ZO-1, occluding and claudin-1 as previously described (Yang et al., 2022).

2.4.3. Biochemical assays and Elisa measurements

The TG and TC levels in serum and liver as well as the activities of AST and ALT in serum were determined with commercial assay kits following the manufacturer's protocols. The concentrations of TNF-α, IL-1β, IL-6 and LPS in liver, and the serum LPS level were assessed using ELISA kits.

2.4.4. Quantitative real-time PCR (qRT-PCR) analysis

Total RNA was isolated from colon using Trizol reagent. The extracted RNA was then subjected to synthesize cDNA using a PrimeScript™ RT Master Mix Kit on a ProFlex™ PCR System (Applied Biosystems, Foster City, CA, USA). The real-time qPCR was conducted in triplicate on a qTOWER 3G (Analytic Jena, Jena, Germany) with TB Green® Premix Ex Taq™ II kit. β-actin was used as control by the $2^{-\Delta\Delta Ct}$ method. The primer sequences of β-actin, ZO-1, occludin, claudin-1, Reg3β and Reg3γ are listed in Table S1.

2.4.5. Gut microbiota assessment

Microbial DNA was extracted from colonic contents according to the instructions of the Fast DNA Spin Kit for Feces. PCR amplification of 16S rRNA gene at V3-V4 region was processed after DNA purity detection. Thereafter, purified amplicons were quantified, pooled and sequenced on an Illumina Miseq platform (Illumina, San Diego, USA). Sequencing data were processed and subjected to bioinformatics analysis using QIIME2 software pipeline (https://qiime2.org) and R (version 4.1.0) packages referring to a previous publication (Li et al., 2021). Linear discriminant analysis effect size (LEfSe) software (LEfSe 1.0) was utilized to determine differentially abundant feature taxa ($p < 0.05$, LDA > 3.5) in response to different treatments based on non-parametric factorial Kruskal-Wallis sum-rank test. Besides, Phylogenetic Investigation of Communities by Reconstruction of Unobserved States (PICRUSt) software (version 1.1.4) was applied to predict gene functions on the basis of Kyoto Encyclopedia of Genes and Genomes (KEGG) database. Spearman correlation coefficients between genera were calculated for gut microbiota co-abundance networks' construction and the networks' visualization was realized using Gephi (version 0.9.7).

2.4.6. SCFAs quantification

The separation and determination of SCFAs were carried out with reference to a previously reported study (Yang et al., 2022). Concisely, 50 mg of colonic contents were homogenized in saturated NaCl solution (500 μL) at 70 Hz for 2 min, and then mixed uniformly with 40 μL of H_2SO_4 (9 %, *v/v*). Next, the above mixture was mixed well with 800 μL of anhydrous ether to acquire SCFAs. The supernatants resulting from centrifugation (12,000 ×*g*, 15 min) was then dehydrated by anhydrous Na_2SO_4, transferred to vials and measured by GC–MS.

2.5. Statistical analysis

Data were presented as mean ± standard deviation (SD). One-way

ANOVA accompanied by *post-hoc* multiple comparisons (Fisher's least significant difference test) was performed using GraphPad Prism version 8.0 (GraphPad Software, La Jolla, CA, USA). Statistically significant was considered at $p < 0.05$.

3. Results

3.1. Mw and monosaccharide composition analyses

HJPS elution profiles on a DEAE Sepharose Fast Flow ion-exchange column and a Sephadex G-50 gel column are illustrated in Fig. 1A and B, respectively. After two-step purification, HJPS1–2 which accounted for approximately 87.23 % of total crude HJPS mass, was separated for succedent structure identification and bioactivity investigation. The total carbohydrate and protein contents of HJPS1–2 were 93.85 % and 1.64 %, respectively. Clearly, a single narrow peak observed in HPGFC chromatogram (Fig. 1C) indicated that HJPS1–2 was relatively homogeneous and pure, with an average Mw of 3.49 kDa. HPAEC chromatograms of HJPS1–2 and the mixture standard (Fig. 1D, Table S2) demonstrated that HJPS1–2 was comprised of Ara, Gal, Glc, Xyl and Man with a molar ratio of 6.83:1:417.17:8.75:1.25 (1.57 %:0.23 %:95.90 %:2.01 %:0.29 %), and Glc was apparently the dominant monosaccharide in isolated HJPS1–2.

3.2. Methylation and NMR spectroscopy analyses

Further structural information of HJPS1–2 referring to main sugar residues and their substituted positions was identified through methylation and GC–MS determinations. The GC–MS chromatogram and respective EI-MS spectra of PMAAs are displayed in Figs. 1E and S1, respectively. Additionally, inferred linkage modes and molar ratio percentages of glycosyl units are listed in Table 1. The results revealed that HJPS1–2 contained 90.59 % glucopyranosyl residues and this ratio approximated monosaccharide composition data. Significantly, HJPS1–2 primarily consisted of four linkage patterns, including Glcp-(1 →, → 4)-Glcp-(1 →, → 6-Glcp-(1 →, and → 4,6)-Glcp-(1 → with a molar ratio of 12.03: 48.33: 7.68: 20.73. Among them, the branching points (1,4,6-linked α-Glc) occupied 23.35 % of total glycosyl residues, inferring a highly branched backbone of HJPS1–2.

NMR spectroscopy was employed to elucidate more detailed structural features of HJPS1–2 (Figs. 2 and 3). In ^{1}H NMR spectrum (Fig. 2A), anomeric proton signals locating at δ5.32, 4.89, 5.26, 4.92, 5.16 and 4.58 denoted six distinct sugar residues arbitrarily labeled as letters from A to F. Correspondingly, anomeric carbon signals were captured at δ101.15/5.32, 99.54/4.89, 101.33/5.26, 100.22/4.92, 93.36/5.16 and 97.24/4.58 in ^{13}C NMR spectrum (Fig. 2C) on the basis of cross-peaks in HSQC spectrum (Fig. 3B). Additionally, typical C6 chemical shift signals were identified at δ68.46, 67.44, 62.17, 62.03, 62.03 and 61.96 in DEPT–135 spectrum (Fig. 2B). According to neighboring correlations in ^{1}H-^{1}H COSY spectrum (Fig. 3A), three cross-peaks at δ5.32/3.57, 3.57/3.90 and 3.90/3.59 revealed that H1–H4 signals of residue A located at δ5.32, 3.57, 3.90 and 3.59. Subsequently, corresponding C1–C4 chemical shifts at δ101.15, 72.92, 74.54 and 78.32 were readily deduced from HSQC spectrum (Fig. 3B). In NOESY spectrum (Fig. 3C), H1 of residue A exhibited associations with peaks at δ3.59, 3.79 and 3.90, indicating H5 chemical shift at δ3.79. Then, cross-coupling resonance signals detected in HSQC spectrum at δ3.79/72.76 and δ3.79, 3.71/61.96 were assigned to H5/C5 and H6a, H6b/C6 of residue A. The above shifts corresponded nearly to the literature data (Guo et al., 2020; Ma et al., 2022; Wang et al., 2021), suggesting that residue A was attributed to → 4)-α-D-Glcp-(1 → .

^{1}H NMR spectrum (Fig. 2A) showed a distinctive anomeric proton resonance at δ4.58, implying that residue F was of β-anomeric configuration (Ma et al., 2022). A relatively high-field chemical shift of its corresponding anomeric carbon signal at δ97.24 deduced from a correlation peak in HSQC spectrum (Fig. 3B) revealed an unsubstituted C1 of residue F (Agrawal, 1992). Proton signals of H2 (δ3.20), H3 (δ3.71), H4 (δ3.89), H5 (δ3.59), H6a (δ3.80) and H6b (δ3.71) were obtained based on combined interpretations of ^{1}H-^{1}H COSY and TOCSY spectra (Fig. 3A and E). Besides, corresponding C2–C6 carbon resonances at δ75.47, 77.63, 78.75, 76.00 and 62.03 could be readily attributed according to correlations in HSQC spectrum (Fig. 3B). Notably, the downfield shift of F-C4 supported 4-mono-substitution of residue F (Ma et al., 2022). Considering the complete chemical shifts, residue F may be assigned to → 4)-β-D-Glcp at the reducing terminal end, which was coherent with the literature data (Wu et al., 2022; Yuan et al., 2020). Likewise, the remaining glycosidic bond signals are assigned and summarized in Table 2. It is noteworthy that on account of mutarotation phenomenon of glucose, distinct signals corresponding to α- and β-configurations of (4 →)-linked-D-Glcp interconverting in aqueous solution were captured in 1D and 2D NMR spectra of HJPS1–2. Similar characterized reducing terminal has been well documented in numerous studies (Wu et al., 2022; Xie et al., 2020; Yang et al., 2020; Yuan et al., 2020). Moreover, integration of anomeric signals revealed an approximate molar ratio of sugar residues A, B, C and D of 3.1:1.1:1.3:1 based on literature (Yuan et al., 2020).

HMBC associations (Fig. 3D) of A-H1 with A-C4 (δ5.32/78.32), A-C1 with A-H4 (δ101.15/3.59), A-H1 with B-C4 (δ5.32/77.63), A-C1 with B-H4 (δ101.15/3.53), B-H1 with A-C4 (δ4.89/78.32), B-C1 with A-H4 (δ99.54/3.59), D-H1 with B-C6 (δ4.92/68.46), D-C1 with B-H6a (δ100.22/3.79), D-C1 with B-H6b (δ100.22/3.92), C-C1 with D-H6a (δ101.33/3.92), and C-C1 with D-H6b (δ101.33/3.67) identified glycosidic linkages of → 4)-α-D-Glcp-(1 → 4)-α-D-Glcp-(1 →, → 4)-α-D-Glcp-(1 → 4,6)-α-D-Glcp-(1 →, → 6)-α-D-Glcp-(1 → 4,6)-α-D-Glcp-(1 → and α-D-Glcp-1 → 6)-α-D-Glcp-(1 → (Guo et al., 2020; Teng et al., 2023). The NOESY spectrum (Fig. 3C) showed key correlative signals of (A-H1/A-H4) at δ5.32/3.59, (A-H1/B-H4) at δ5.32/3.53, (B-H1/A-H4) at δ4.89/3.59, (D-H1/B-H6a) at δ4.92/3.79, (D-H1/B-H6b) at δ4.92/3.92, and (C-H1/D-H6a) at δ5.26/3.92, which further confirmed glycosyl linkages of above residues. It should be noted that minor sugar residues such as terminal Araf, terminal Galp, → 4)-Xylp-(1 → and → 2)-Manp-(1 → as detected via methylation analysis, could not be clearly identified

Table 1
Glycosidic linkage composition of methylated HJPS1–2.

	RT (min)	Methylated sugar	Mass fragments (*m/z*)	Molar ratio (%)	Type of linkage
1	10.61	2,3,5-Me$_3$-Araf	43,71,87,101,117,129,145,161	3.03	Araf-(1→
2	15.55	2,3-Me$_2$-Xylp	43,71,87,99,101,117,129,161,189	2.02	→4)-Xylp-(1→
3	17.16	2,3,4,6-Me$_4$-Glcp	43,71,87,101,117,129,145,161,205	12.03	Glcp-(1→
4	17.69	2,3,4,6-Me$_4$-Galp	43,71,87,101,117,129,145,161,205	0.81	Galp-(1→
5	18.15	2-Me$_1$-Araf	43,58,85,99,117,127,159,201	1.21	→3,5)-Araf-(1→
6	21.01	3,4,6-Me3-Manp	43,87,129,161,189	0.61	→2)-Manp-(1→
7	21.73	2,3,6-Me$_3$-Glcp	43,87,99,101,113,117,129,131,161,173,233	48.33	→4)-Glcp-(1→
8	22.39	2,3,4-Me$_3$-Glcp	43,87,99,101,117,129,161,189,233	7.68	→6-Glcp-(1→
9	23.83	2,3,4-Me$_3$-Galp	43,87,99,101,117,129,161,189,233	0.61	→6)-Galp-(1→
10	24.59	2,6-Me$_2$-Glcp	43,87,97,117,159,185	1.82	→3,4)-Glcp-(1→
11	26.95	2,3-Me$_2$-Glcp	43,71,85,87,99,101,117,127,159,161,201	20.73	→4,6)-Glcp-(1→
12	30.40	2,4-Me2-Galp	43,87,117,129,159,189,233	1.11	→3,6)-Galp-(1→

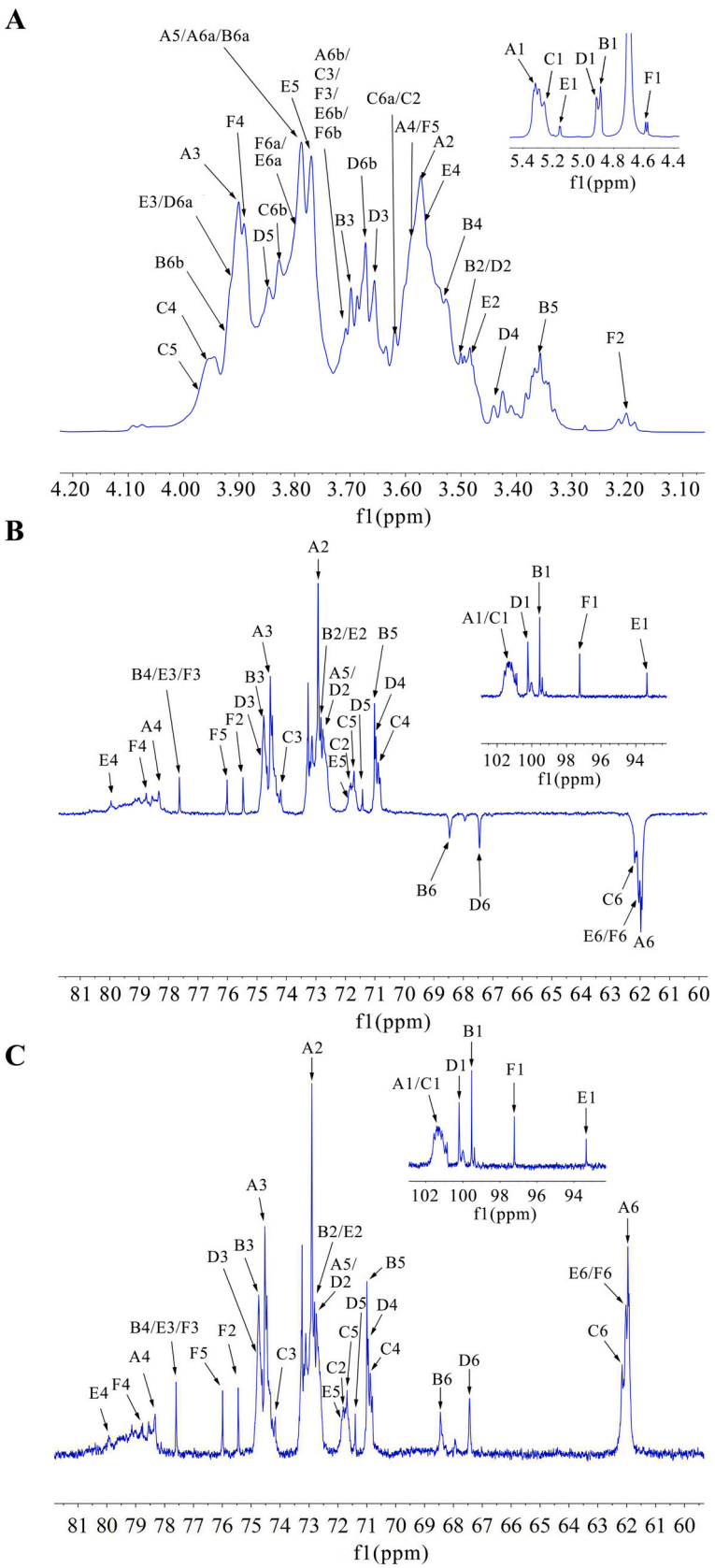

Fig. 2. 1D NMR spectra of HJPS1–2. (A) ^{1}H NMR; (B) DEPT-135; (C) ^{13}C NMR.

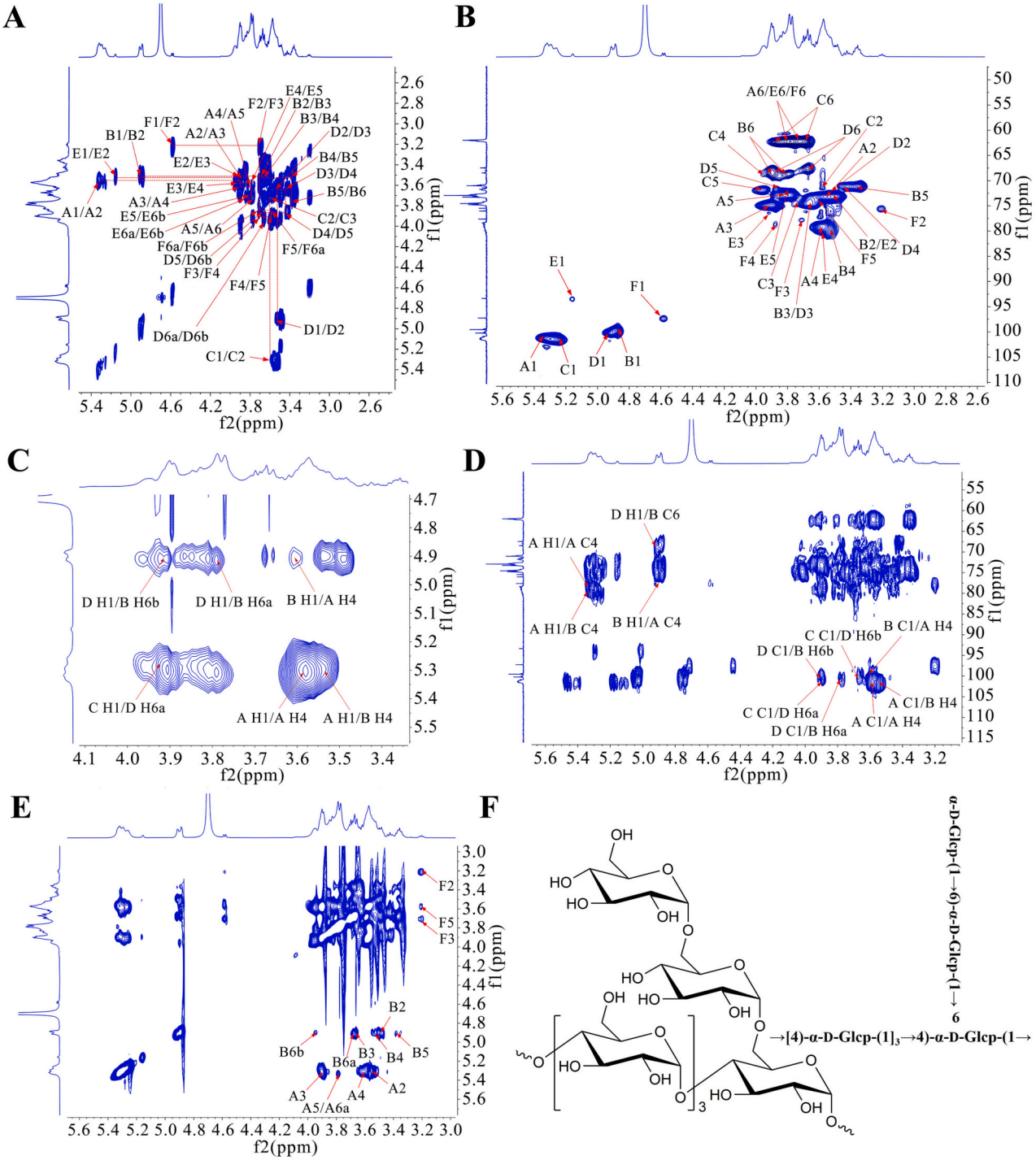

Fig. 3. 2D NMR spectra of HJPS1–2. (A) ^{1}H-^{1}H COSY; (B) ^{1}H-^{13}C HSQC; (C) ^{1}H-^{1}H NOESY; (D) ^{1}H-^{13}C HMBC; (E) ^{1}H-^{1}H TOCSY; (F) Predicted chemical structure of the repeating unit of HJPS1–2.

and assigned in the NMR analysis due to their low abundance. Furthermore, detailed inspection and careful verification of spectroscopic signals in 2D NMR spectra disclosed that these sugar residues at trace amounts had no associations with glucopyranosyl residues A–F, thus confirming separate components. In short, combined with the results of Mw (3.49 kDa), monosaccharide composition and methylation analyses, the major component in HJPS1–2 was found to be a short-chain branched α-D-glucan and the speculative structure of its repeating unit could be proposed as shown in Fig. 3F.

3.3. Body weight, liver index and liver morphology

There was no significant difference in mice body weight among the groups prior to experiment ($p > 0.05$, not shown), but it was remarkably lighter in the EtOH group compared to that in the Ctrl group at the end of dietary intervention (Fig. 4B). Besides, EtOH feeding resulted in a dramatic increment in liver index relative to the Ctrl group (Fig. 4C). Obviously, HJPS administration strikingly increased the body weight and decreased the liver index of EtOH-fed mice, with no significant difference between low and high doses of HJPS ($p > 0.05$). Moreover,

Table 2
^{1}H and ^{13}C NMR chemical shifts[a] of HJPS1–2 in D_2O (δ4.70) at 295 K.

Glycosyl residues	H1/C1	H2/C2	H3/C3	H4/C4	H5/C5	H6a/C6	H6b
A → 4)-α-D-	5.32	3.57	3.90	3.59	3.79	3.79	3.71
Glcp-(1→	101.15	72.92	74.54	78.32	72.76	61.96	
B → 4,6)-α-D-	4.89	3.50	3.70	3.53	3.36	3.79	3.92
Glcp-(1→	99.54	72.82	74.76	77.63	71.00	68.46	
C α-D-Glcp-	5.26	3.62	3.71	3.96	3.98	3.62	3.83
1→	101.33	71.85	74.18	70.89	71.70	62.17	
D → 6)-α-D-	4.92	3.50	3.66	3.44	3.85	3.92	3.67
Glcp-(1→	100.22	72.76	74.80	70.96	71.41	67.44	
E → 4)-α-D-	5.16	3.49	3.92	3.56	3.77	3.80	3.71
Glcp	93.36	72.82	77.63	79.95	71.93	62.03	
F → 4)-β-D-	4.58	3.20	3.71	3.89	3.59	3.80	3.71
Glcp	97.24	75.47	77.63	78.75	76.00	62.03	

[a] ^{1}H and ^{13}C NMR chemical shift assignments of HJPS1–2 relative to a solvent peak (δ4.79 for D_2O) and an internal standard (δ30.20 for the methyl carbon signal of acetone) (Silveira et al., 2014) were shown in Table S3, Supplementary Material.

representative pathological micrographs of mice liver illustrated that EtOH exposure led to apparent hepatic lesions as attested by swelling, deformation and vacuolar degeneration of hepatocytes, occasionally punctate infiltration of inflammatory cells, as well as severe deposition of lipid droplet compared with the Ctrl group (Fig. 4M). However, markedly reduced hepatocytes' vacuolization, suppressed lipid accumulation, together with eliminated inflammation in HJPS-fed and PC-treated mice relative to the EtOH group implied the reversal of hepatic impairment. Furthermore, remarkable discrepancies were observed in relieving effects of HJPS-L and HJPS-H on EtOH-induced liver injury.

3.4. HJPS facilitated the resolution of aberrant biochemical parameters and hepatic inflammation

The EtOH group presented dramatically higher TC and TG concentrations in murine serum and liver than those in the Ctrl group (Fig. 4D–G), suggesting the occurrence of dyslipidemia. Both doses of HJPS administration exhibited great capabilities to inhibit lipid accumulation. In particular, HJPS-L and HJPS-H showed similar abilities in reducing serum TG, liver TC and TG. Several enzymes in serum were used as biochemical markers of early liver damage. Serum ALT and AST activities remarkably ascended in EtOH-treated mice compared with those in the Ctrl group, indicating the appearance of hepatocyte damage (Fig. 4H and I). It was worth noting that the inhibitory effect of HJPS-H on the elevation of serum ALT and AST was stronger than that of HJPS-L, which was similar to that of PC. Moreover, the EtOH group presented a striking elevation in hepatic TNF-α, IL-6 and IL-1β levels relative to the Ctrl group, which were pronouncedly suppressed after HJPS and silymarin supplementations (Fig. 4J–L). Intriguingly, both doses of HJPS intervention restored hepatic inflammatory factors to normal levels, inferring a potential anti-inflammatory effect of HJPS in ALD mice.

3.5. HJPS restored healthy intestinal morphology and barrier function

Histopathology examinations of mice ileum and colon were conducted by H&E staining (Fig. 4N). Slight ileum damage was noticed in the EtOH group, mainly reflected in necrosis and exfoliation of a part of epithelial cells, as well as mild edema, loose arrangement of connective tissue and mild dilatation of capillaries in the submucosa. Accordingly, EtOH ingestion led to occasional disappearance of intestinal glands, replaced by hyperplastic connective tissue with minimal lymphocyte infiltration, as observed in colonic section images. Notably, a dose-response relationship of HJPS intervention was found on alleviation of EtOH-induced intestinal injury. Explicit and complete mucosal structure of ileum and colon without any visible inflammatory alterations was noted in HJPS-H-treated mice. Consequently, it was speculated that HJPS treatment might repair EtOH-impaired intestinal morphology through enhancing the absorption of intestinal nutrients and promoting intestinal development.

Meanwhile, immunofluorescence (Fig. 5H) and RT-qPCR analyses (Fig. 5A–C) disclosed that the fluorescence intensity and mRNA expression levels of ZO-1, occludin and claudin-1 in murine ileum dramatically descended after EtOH administration, implying a striking loss of intestinal barrier integrity, which was effectively reversed by both doses of HJPS intervention. Consistently, HJPS-H supplementation conspicuously inhibited EtOH-caused reduction of mRNA expression levels of antimicrobial peptides Reg3β and Reg3γ in mice ileum (Fig. 5D and E). To further verify the enhancement effect of HJPS on intestinal barrier function, LPS contents in mice serum and liver were determined. As depicted in Fig. 5F and G, EtOH exposure pronouncedly elevated circulating and hepatic levels of LPS, whereas these aberrant shifts were restored to levels comparable to the Ctrl group by HJPS and silymarin treatments. Collectively, two doses of HJPS administration might play a key role in maintaining intestinal homeostasis in EtOH-fed mice.

3.6. HJPS rescued compromised microbiota

Markedly α-diversity alterations in response to various treatments were seen in Fig. 6A, mainly manifested as descending richness (Chao1) and ascending diversity (Shannon & Simpson indexes) of gut microbiota after EtOH feeding, which were remarkably reversed by HJPS-H intake. PCoA analysis based on dissimilarities of weighed unifrac distance identified a high degree of variations among different groups, especially a distinct clustering between Ctrl and EtOH groups, in accordance with the results of NMDS analysis (Fig. 6B). PCoA1 completely separated the HJPS-H group from the EtOH group. Meanwhile, HJPS-H appeared to be more effective than silymarin in reconstructing EtOH-disrupted gut microbiota structure. Anosim and Adonis analyses revealed significant differences ($p < 0.05$) among the groups and corroborated great contributions of EtOH or HJPS interventions to the considerable dissimilarities (Table S4).

Gut microbiota composition of different groups is displayed in Fig. 6C–E and S2. Compared with the Ctrl group, EtOH dramatically elevated the relative abundance of Bacteroidota and Proteobacteria, whereas it conspicuously decreased the colonization of Verrucomicrobiota, Firmicutes and Actinobacteriota at the phylum level (Fig. 6D). Nevertheless, this anomaly was dramatically reversed by HJPS-H ingestion, especially reflected in remarkably restored ratio of Firmicutes to Bacteroidota (F/B) (Fig. 6D). The identification of differential taxa at genus level in response to EtOH and HJPS-H treatments was conducted by LEfSe analysis between Ctrl and EtOH groups (Fig. S2), as well as that between EtOH and HJPS-H groups (Fig. 6E), respectively. The results illustrated that compared with the Ctrl group, EtOH markedly enhanced the prevalence of genus *Alistipes*, *Alloprevotella*, *Bacteroides*, *Muribaculaceae*, *Mucispirillum*, *Parabacteroides*, *Rikenellaceae RC9 gut group* and *Azospirillum*, which was strikingly restricted after HJPS-H intervention (Figs. 6E and S2). Meanwhile, the relative abundance of genus *Akkermansia* and *Eubacterium coprostanoligenes group* considerably reduced after EtOH intake, and this trend was notably reversed in HJPS-H group (Figs. 6E and S2). Overall, HJPS-H administration had the potential to considerably ameliorate EtOH-induced disturbance of specific gut microbial communities.

3.7. HJPS improved the predicted functional profiles and co-occurrence networks of gut microbiome

The functional profiles of gut microbiota were predicted by PICRUSt assessment (Fig. 7). Comparisons of level-2 KEGG pathways disclosed that the functional performances of HJPS-H group were clustered closer to the Ctrl group than that to the EtOH group, specifically manifested as descending levels of potential infectious diseases, neurodegenerative diseases and metabolic diseases, as well as enhancement of amino acid

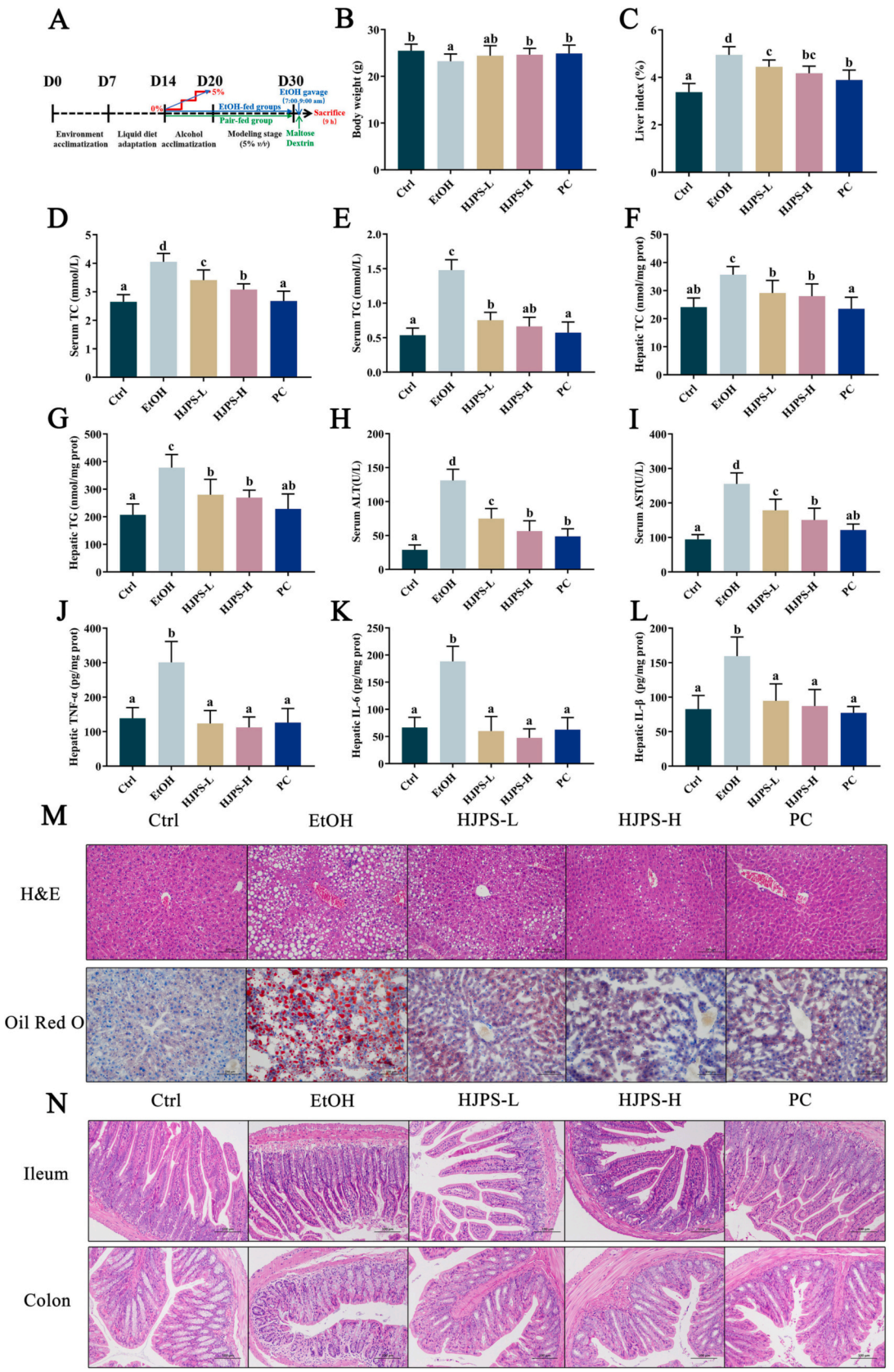

Fig. 4. Effect of HJPS1–2 supplementation on ALD-related indicators in mice. (A) Schematic diagram of the animal experimental design; (B) Body weight; (C) Liver index; (D&E) Levels of serum TC and TG; (F&G) Levels of hepatic TC and TG; (H&I) Levels of serum ALT and AST; (J-L) Hepatic TNF-α, IL-6 and IL-1β levels; (M&N) Histological analyses of murine liver, ileum and colon (200× magnification). Bar plots are expressed as mean ± SD ($n = 10$). Different lowercase letters denote statistically significant differences ($p < 0.05$) between the groups.

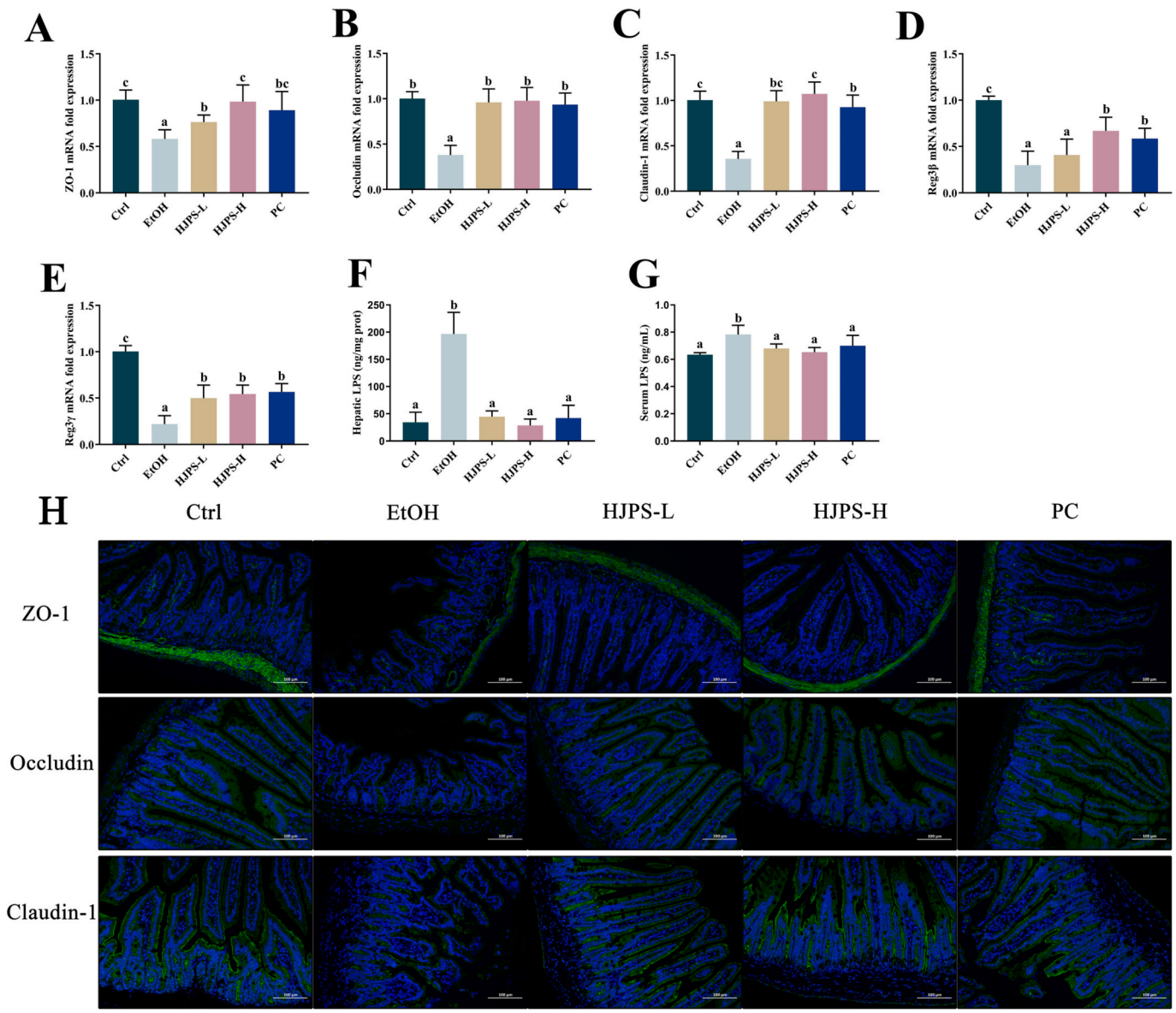

Fig. 5. Effect of HJPS1–2 intervention on intestinal barrier function in mice. The RNA expression levels of ileum ZO-1 (A), occludin (B), claudin-1 (C), Reg3β (D)and Reg3γ (E) were determined by RT-qPCR using β-actin as an internal control. (F&G) Levels of hepatic and serum LPS. (H) Representative images of immunofluorescence analysis of ZO-1, occludin and claudin-1 (green) in ileum of mice. Nuclei were stained with DAPI (blue). Magnification ×200. Bar plots are shown as mean ± SD ($n = 10$). Different lowercase letters indicate statistically significant differences ($p < 0.05$) between the groups. (For interpretation of the references to color in this figure legend, the reader is referred to the web version of this article.)

metabolism, metabolism of terpenoids and polyketides, environmental adaptation, membrane transport and lipid metabolism levels in HJPS-H group relative to the EtOH group, which confirmed the conducive role of HJPS-H in regulating gut microbiota.

Gut microbiota symbiotic networks at genus level under various interventions are depicted in Fig. 8 and accordingly topological features are summarized in Table S5. Notably, the degree distribution histogram of nodes in the Ctrl group conformed to the power law model, while it in the EtOH group fitted the Poisson model, implying the transformation of co-occurrence network from a scale-free network to a random graph after excessive alcohol exposure. Besides, 10, 4, 7, 7 and 7 modules of co-enriched taxa were identified in networks of Ctrl, EtOH, HJPS-L, HJPS-H and PC groups, respectively. The maximum number of modules detected in the Ctrl group reflected the sparsity of the correlation network. In contrast, the co-abundance network of the EtOH group was larger and more complex in comparison with that of the Ctrl group, as evidenced by profound increments of nodes, edges, average degree and average clustering coefficient, as well as a decrement in average path length, suggesting remarkably altered topological characteristics of microbial interaction network caused by EtOH intake. The synergistic and antagonistic relationships among gut microbes in the Ctrl group maintained a relative balance, whereas microbial interactions in the EtOH group were dominated by synergy, which could partially explain a higher microbial diversity (Shannon & Simpson indexes, Fig. 6A) of EtOH group. Interestingly, the synergistic and antagonistic relationships among microorganisms tended to rebalance after HJPS-H supplementation relative to EtOH intervention, and the density of bacterial association network decreased, as attested by the reduction of nodes and links, as well as the elevation of module count and average path length.

3.8. HJPS restored intestinal SCFA levels

SCFAs' Levels in mice colonic contents were measured (Fig. 9). EtOH consumption prominently decreased seven SCFAs' levels in comparison

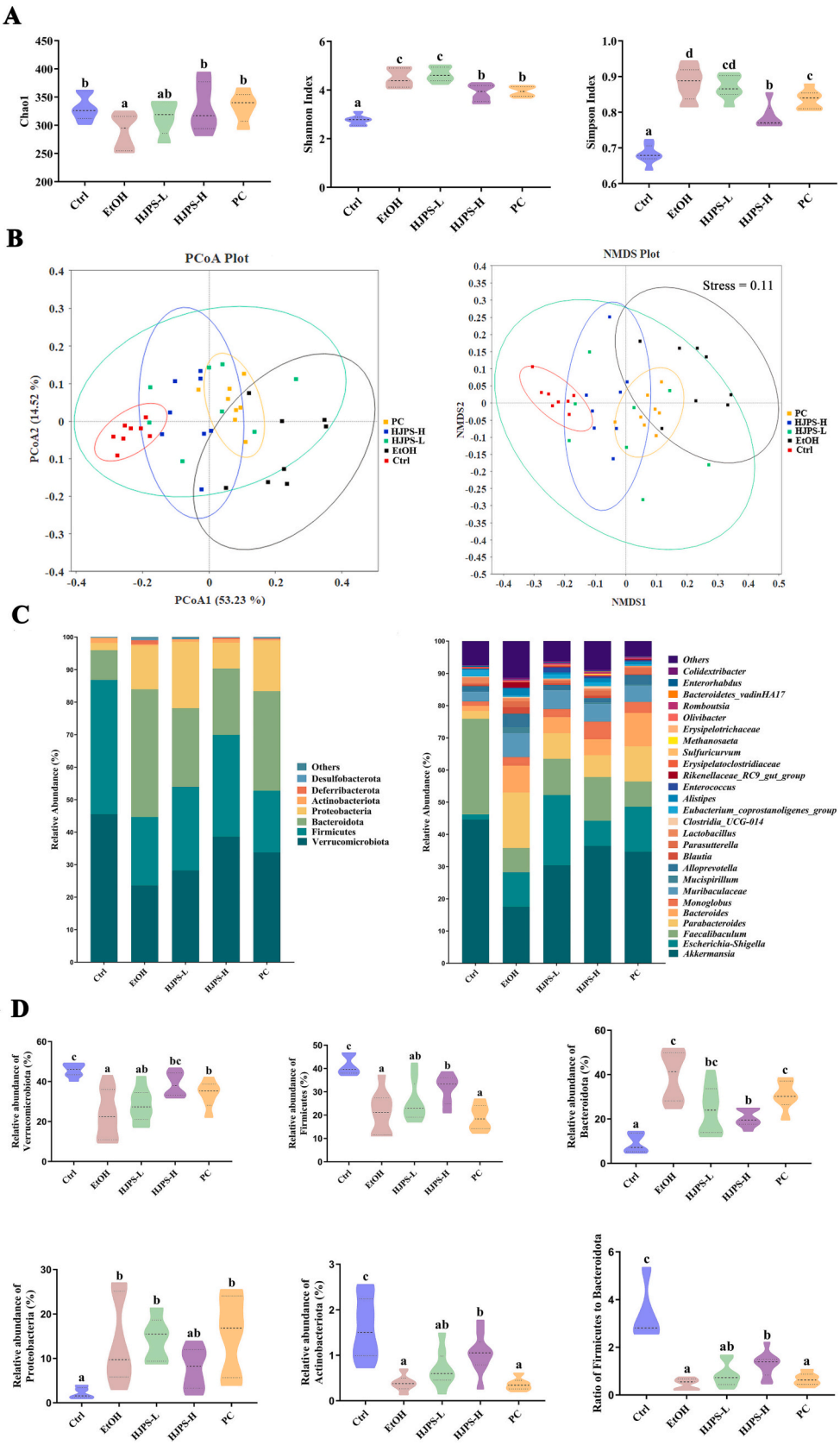

Fig. 6. Microbiome analysis of colonic contents. (A) α-diversity comparisons of Chao1, Shannon and Simpson indexes, respectively; (B) PCoA and NMDS plots illustrating overall distribution patterns of gut microbiota calculated using weighed unifrac distance; (C) Stacked diagrams of gut microbiota composition dissimilarities at phylum (left) and genus (right) levels; (D) Comparisons of relative abundance of gut microbial community members at the phylum level among different groups; (E) LEfSe pairwise comparison between EtOH and HJPS-H groups ($p < 0.05$, LDA > 3.5); Values are expressed as mean ± SD ($n = 8$). Different lowercase letters indicate statistically significant differences ($p < 0.05$) between the groups.

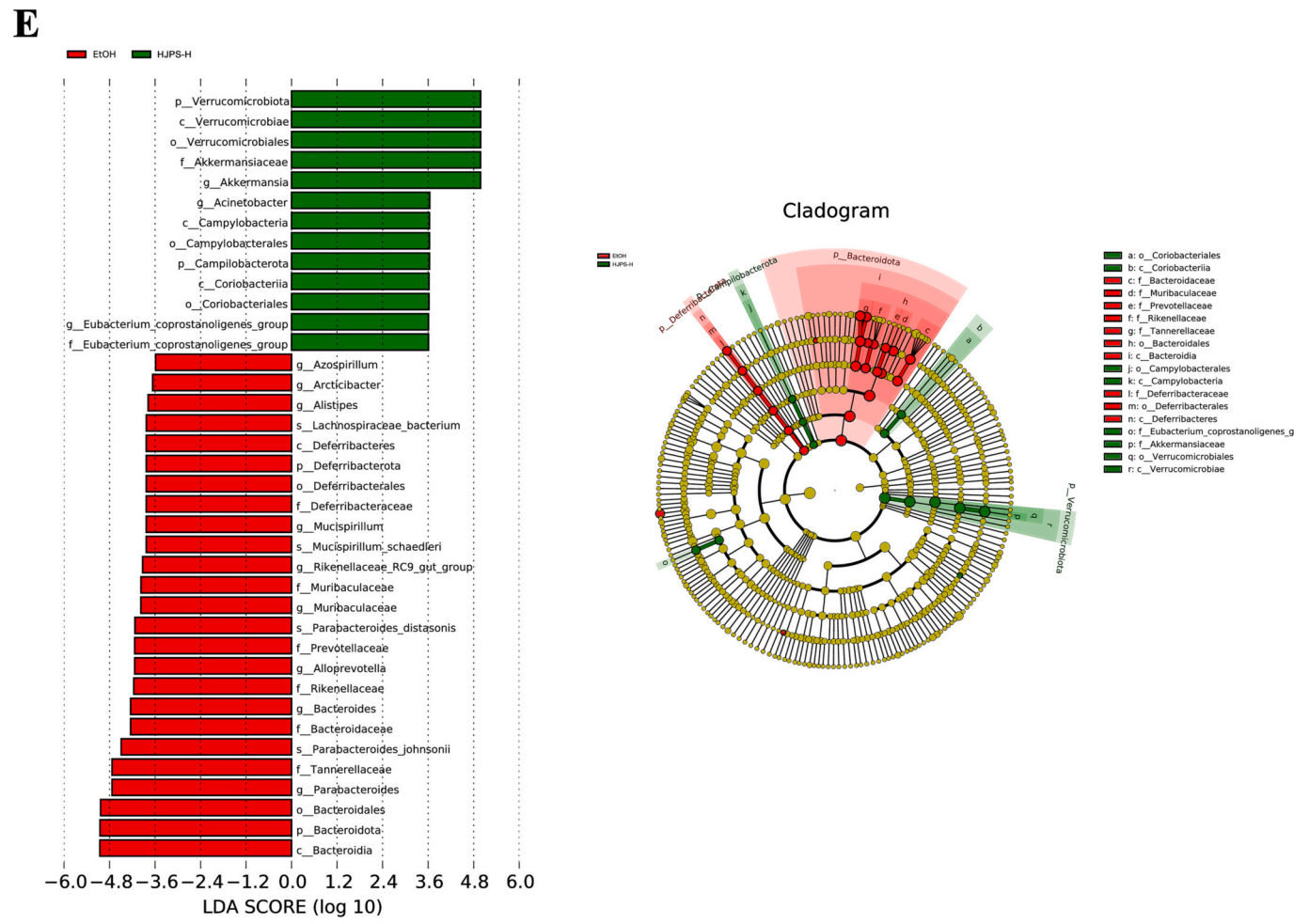

Fig. 6. (*continued*).

to the Ctrl mice, among which the levels of acetic acid, propionic acid, butyric acid and isovaleric acid were conspicuously elevated after HJPS-H supplementation. Apparently, HJPS had a dose-effect on recovering alcohol-induced reduction of intestinal SCFAs, and HJPS-L intervention remarkably increased only two (butyric acid and isovaleric acid) of the seven SCFAs. Additionally, HJPS-H administration pronouncedly increased the content of total SCFAs compared with EtOH group, which was close to that of PC intervention.

3.9. Associations between key differential phylotypes and ALD-related host parameters

To illustrate the relationship between key differential OTUs and the severity of hepatic injury, a total of 27 key genera in response to EtOH and HJPS-H interventions were screened out via LEfSe analysis between Ctrl and EtOH groups (Fig. S2), as well as that between EtOH and HJPS-H groups (Fig. 6E), to construct spearman correlations with ALD-associated indexes, and the results were visualized as shown in Fig. 10. Genus of *Conexibacter*, *Parabacteroides*, *Rikenellaceae RC9 gut group*, and *Alistipes* exhibited a pronouncedly positive association with a clustering of liver biochemical criterions, proinflammatory cytokines and LPS levels, while these genera presented a conspicuously negative correlation with tight junction (TJ) proteins, antimicrobial peptides, acetic acid, propanoic acid, butyric acid, isovaleric acid, hexanoic acid and total SCFAs. Consistently, a markedly opposite correlation was observed for *Mucispirillum*, *Muribaculaceae*, *Arcticibacter*, and *Azospirillum* with intestinal barrier-related proteins, butyric acid, isovaleric acid, hexanoic acid and total SCFAs. In contrast, these microbes showed a tightly positive association with multiple hepatic biochemical data, suggesting their underlying impacts on accelerating pathological progression of ALD. Of note, *Akkermansia*, *Eubacterium coprostanoligenes group* and *Faecalibaculum* were inversely correlated with hepatic biomarkers and LPS concentrations, whereas positively associated with intestinal barrier-related indices, butyric acid, isobutyric acid, isovaleric acid and total SCFAs, inferring the favorable role of these microbes played in attenuating ALD.

4. Discussion

In recent decades, ALD, an inducement of a range of diseases, has been widely recognized as one of the leading causes of liver-related death worldwide (Li et al., 2021). Polysaccharides from a wide array of sources have been deeply investigated to possess multiple pharmacological activities, especially effective hepatoprotective activity (Yang, Wu, et al., 2020). Although available evidence confirms underlying functional properties of HJPS (Peng et al., 2019; Shen et al., 2015), more comprehensive structural information and in-depth bioactivities evaluation *in vivo* are still limited. Hence, in this study, HJPS1–2 was successfully prepared via EtOH precipitation, protein elimination and two-step purification for structure exploration and hepatoprotective activity verification. Structure identification revealed that HJPS1–2 was mainly a homogeneous α-glucan with an average Mw of 3.49 kDa. The predicated repeating unit structure of HJPS1–2 was → 4)-α-D-Glcp-(1 → as the major backbone, and α-D-Glcp-(1 → 6)-α-D-Glcp-(1 → linked at O-6 position of → 4,6)-α-D-Glcp-(1 → as the side chain. Meanwhile, each structural repeating unit contained a main chain of four glucose residues

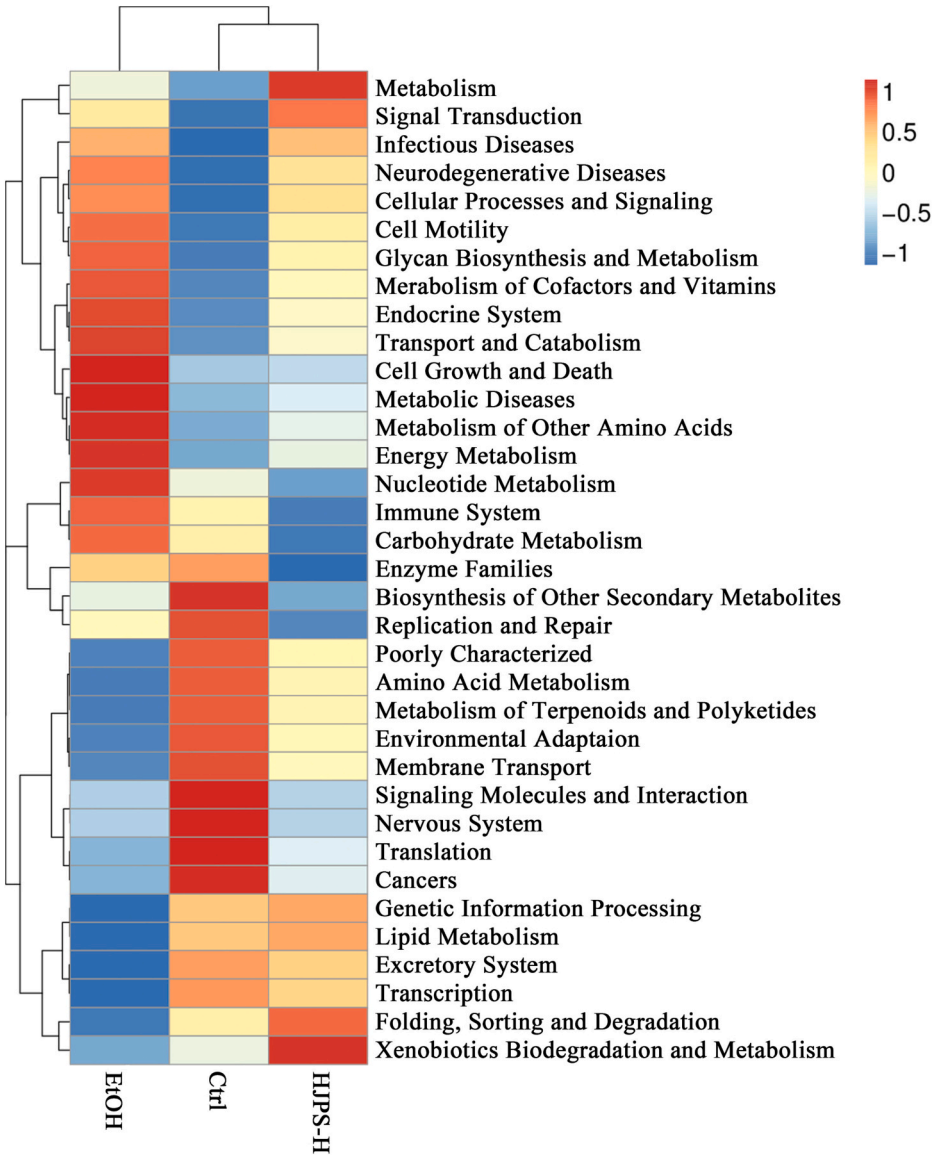

Fig. 7. The heatmap of PICRUSt analysis at level 2 concerning the prediction of metagenomic functions and the clustering from dissimilarity levels of top 35 abundant gene functions.

and a branched chain. At present, resolving of polysaccharides structure-activity correlations remains the focus of considerable scientific research, and existing evidence supports that regular structural characteristics of polysaccharides, including Mw, degree of branching, chain conformation, configuration, glycosidic bonds, monosaccharide composition and functional groups, are likely to be intrinsic and vital factors contributing to their bioactivities (Cai, Zou, Liang, & Luan, 2018; Jiang et al., 2022; Teng et al., 2023). Among them, Mw is generally considered to exert specific effects on polysaccharides' hepatoprotective activities (Cai et al., 2018; Huang et al., 2016). Two of the four polysaccharide fractions extracted from *Agaricus bisporus* industrial wastewater with lower Mw were found to exhibit more pronounced restorative effects on CCl_4-induced elevation of murine ALT and AST levels (Huang et al., 2016). Cai et al. (2018) reported that compared with STRP2, STRP1 with relatively lower Mw from *Sophorae tonkinensis Radix* showed more potent hepatoprotective activity in a mouse model of acetaminophen-induced hepatic injury. Similarly, polysaccharides with a low Mw, such as mycelia zinc polysaccharide MZPS-1 with Mw of 4.6 kDa from *Pleurotus djamor* (Zhang et al., 2016) and chicory polysaccharide CP-1 with Mw of 8.5 kDa from *Cichorium intybus* L. roots (Wu et al., 2018), were reported to present great hepatoprotective effect *in vivo*. Moreover, the highly branched fine structure of glucans is also thought to be crucial for their bioactivities (Luo et al., 2022; Takaya et al., 1998; Wang et al., 2021). One study disclosed that scallop glucans with highly branched and short chains tended to exhibit remarkable immunomodulatory effect (Takaya et al., 1998). HPP-1S with prominent antitumor efficacy was found in the gonads of *Hemicentrotus pulcherrimus* and presented a linear backbone of α(1 → 4)-D-Glc alternately substituted with α(1 → 6)-D-Glc and α(1 → 6)-D-GlcA at O6-position (Jiang et al., 2022). Of note, an analogous regularity was noted in terms of hepatoprotective activity. A comparison of two polysaccharides derived from *Toona sinensis* leaves revealed that TSP-1 substituted by four branches displayed improved hepatoprotective activity relative to TSP-2 with only two side chains (Cao et al., 2019), which implied that more branches distributed might correspond to higher hepatoprotective activity. Xu et al. (2007) isolated a 1,4-linked α-D-glucan MP-1 from *M. coruscus*, which was protective against CCl_4-induced liver injury, and its structure was characterized by a single α-D-Glcp-(1 → side chain connected at O6-position for every nine monosaccharides along the main chain. Likewise, oral supplementation of mussel α-D-glucan MP-A, with

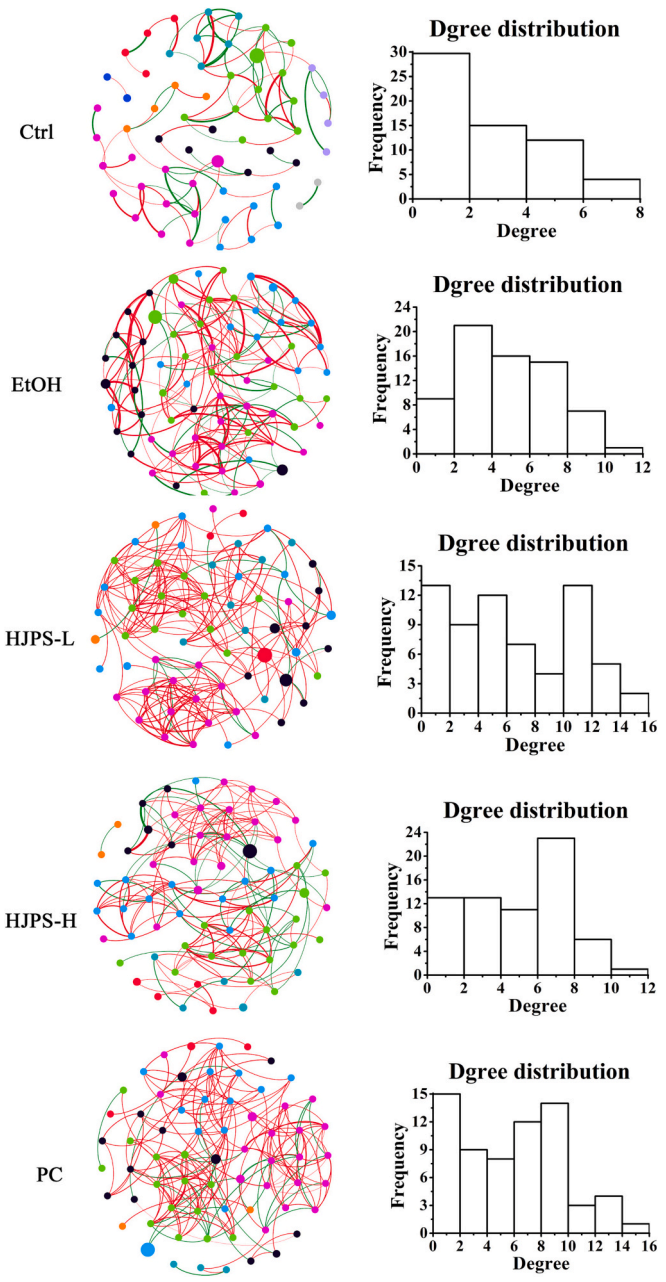

Fig. 8. Co-occurrence network diagrams of gut microbiota. Different nodes represent distinct genera, and the nodes' color is in accordance with the modularity class. The nodes' size indicates average relative abundance of genus. The thickness of nodes' links is positively correlated with an absolute value of spearman correlation coefficient of interactions among different genera. Correlations >0.6 or lower than −0.6 as well as genera abundance >0.01 % were visualized. Red and green connecting lines correspond to the positive and negative correlations, respectively. (For interpretation of the references to color in this figure legend, the reader is referred to the web version of this article.)

a linear α-(1 → 4) linked glucose main chain and one 1,2-α-D-glucose side chain grafted on the backbone every twelve glucose residues, could prevent non-alcoholic fatty liver disease in rats (Wu et al., 2019). Importantly, a polysaccharide purified from *Morchella esculenta* named MEP2 was discovered to had a repetitive structural unit of α-(1 → 4) linked gluconic backbone branched with α-D-Glcp-(1 → 4)-α-D-Glcp-(1 → and α-D-Glcp-(1 → residues at O-6 position, and was proved to be effective in improving ALD (Teng et al., 2023). Of interest, the structure of HJPS1–2 was similar to that of above reported functional polysaccharides, and its low Mw, glycosidic bond composition of side chains, and dense branching configuration (one branch per 4 residues) endowed HJPS1–2 with particularity. Consequently, it was speculated that HJPS1–2 might play a certain role in recovery of EtOH-induced liver damage.

Thereafter, an ALD mouse model was constructed to examine the potential hepatoprotective efficacy of HJPS1–2. As expected, both doses of HJPS treatment effectively restrained raises of liver index and liver function indicators resulted from EtOH exposure (Fig. 4B–I). Besides, HJPS-H showed better bioactivity than HJPS-L in recovery of serum TC and transaminase levels. Liver histopathological assessment indicated that HJPS intervention dose-dependently refined hepatic morphological and structural lesions triggered by EtOH consumption (Fig. 4M), confirming the mitigation effect of HJPS on ALD.

Overwhelming evidence emphasized intimate associations between intestinal barrier dysfunction and the severity of endotoxemia and ALD (Li et al., 2021; Xia et al., 2020). As a crucial part of intestinal mechanical barrier, TJs and their related proteins, including transmembrane proteins (such as claudins and occludin) and cytoplasmic scaffolding proteins (such as ZO-1), were responsible for imparting and retaining polarity of intestinal epithelial cells as well as regulating barrier selective permeability (Bhat et al., 2019). Furthermore, antimicrobial lectins secreted by intestinal epithelial cells, such as regenerating islet-derived proteins (reg3β and reg3γ), played vital roles in innate host defense, including confining the accumulation of bacterial symbiotes, preserving the homeostasis of symbiotic bacteria, and promoting the separation of microbiota from the host (Xia et al., 2020). In the current study, excessive EtOH intake caused mild pathological changes in both ileum and colon and remarkably suppressed mRNA expression levels of ZO-1, occludin, claudin-1, reg3β and reg3γ, while HJPS treatment markedly alleviated these disorders (Figs. 4N and 5A–E). Intestinal barrier integrity impairment was usually accompanied by translocation of PAMPs, such as LPS, peptidoglycan and viral RNA, and activation of downstream pro-inflammatory cascade reactions (Fang et al., 2019). A similar phenomenon was discovered in this study, where LPS levels in both circulation and liver of EtOH-fed mice obviously ascended, followed by dramatic increments in hepatic TNF-α, IL-6 and IL-1β levels (Figs. 5F, G and 4J–L), whereas these indices were restrained to normal levels after both HJPS-L and HJPS-H interferences. An α-(1 → 4) linked glucan WLY-0 with residues at O-6 from Huangshui, a main by-product of Baijiu, was found to be capable of inhibiting pro-inflammatory factors' secretion and upregulating TJ proteins' expressions in LPS-stimulated Caco-2 cells (Huo et al., 2022), which was consistent with our results. Analogously, an α-D-glucan YCP separated from mycelium of marine fungus could reinstate mucosal barrier and rebuild intestinal immune homeostasis in colitis mice, which concretely presented as strikingly upregulated expressions of mucin-2 and two TJ proteins in colon, as well as pronouncedly ascending anti-inflammatory cytokine levels and descending proinflammatory cytokine contents in colon and mesenteric lymph nodes (Liu et al., 2020). Taken together, HJPS might also exert positive effects on repairing intestinal barrier, reducing circulating endotoxin levels and suppressing hepatic inflammation, thus attenuating the progression of ALD.

Gut microbiota dysbiosis, a prominent feature of EtOH abuse, could induce intestinal barrier dysfunction and promote ALD development (Teng et al., 2023). Herein, HJPS dose-dependently reversed EtOH-induced adverse shifts in α-diversity, β-diversity and phylum-level gut flora composition (Fig. 6A–D), particularly characterized by pronouncedly reduced ratio of F/B (Fig. 6D) as previously reported (Ji et al., 2021; Liu, Luo, et al., 2020), which was considered to be an indicator of intestinal dysbiosis and of great importance for modulating host metabolism and immunity (Ji et al., 2021; Li et al., 2022; Ying et al., 2020). Additionally, EtOH-disturbed genus-level signature microbiota including considerably enriched *Alistipes*, *Bacteroides*, *Mucispirillum*, *Parabacteroides* and *Azospirillum*, and profoundly reduced proportion of *Akkermansia* and *Eubacterium coprostanoligenes group*, was conspicuously corrected by HJPS-H supplementation (Figs. 6E and S2). In detail, the

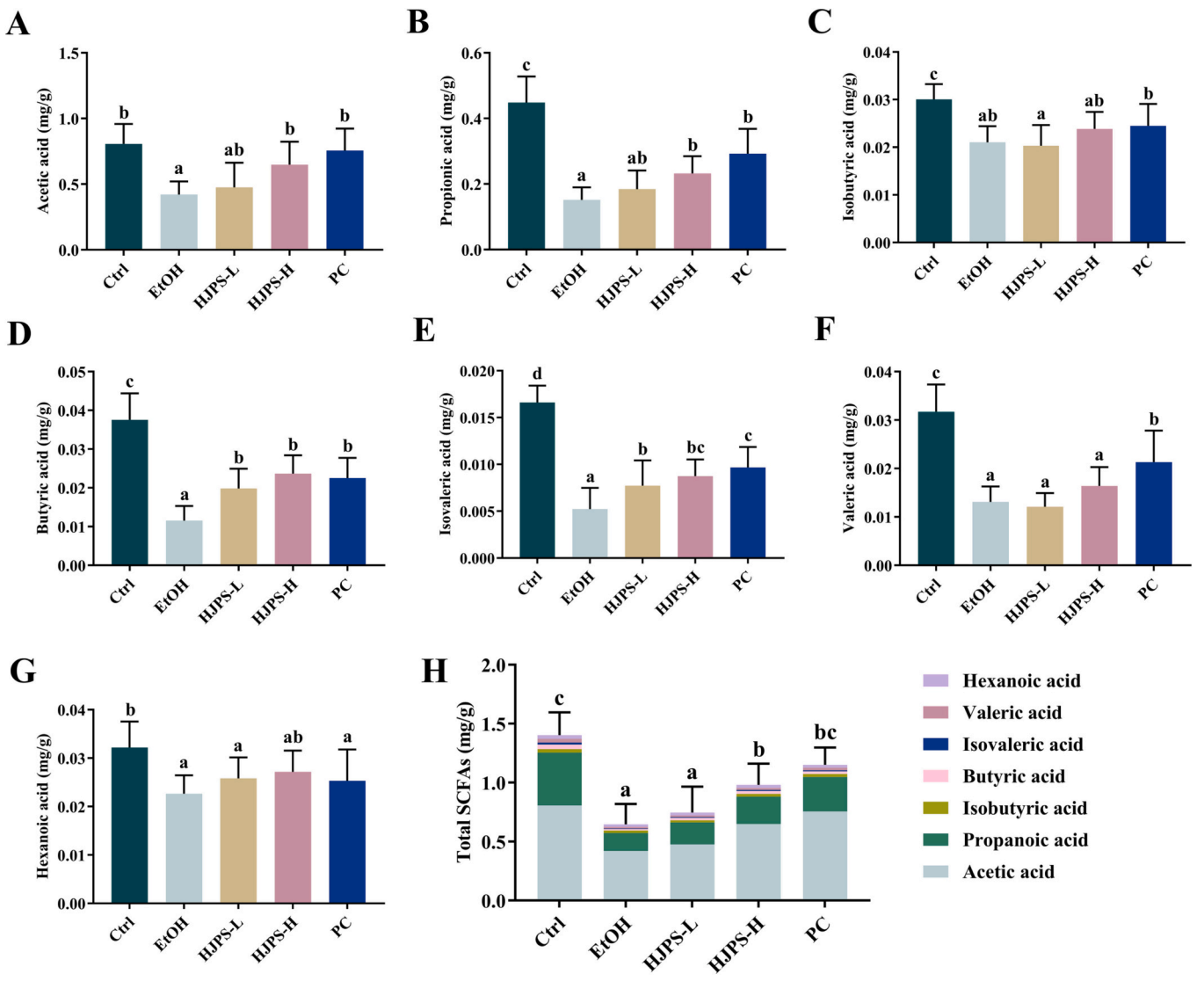

Fig. 9. Effect of HJPS1–2 treatment on SCFAs levels in colonic contents. (A) Acetic acid; (B) propionic acid; (C) isobutyric acid; (D) butyric acid; (E) isovaleric acid; (F) valeric acid; (G) hexanoic acid and (H) total SCFAs. All data are presented as mean ± SD ($n = 8$). Different lowercase letters denote statistically significant differences ($p < 0.05$) between the groups.

well-controlled proliferation of *Mucispirillum* in HJPS-H group, which was reported to inhibit mucous layer formation and destroy intestinal mucosal barrier (Zhao et al., 2020), might contribute to maintaining intestinal barrier integrity after EtOH exposure. Simultaneously, *Mucispirillum* was observed to be pronouncedly positively associated with hepatic pathophysiological indicators and LPS levels, while exhibited strongly adverse associations with intestinal barrier-related indices (Fig. 10), emphasizing crucial role of *Mucispirillum* in ALD development. Alarmingly, abundant *Bacteroides* and *Mucispirillum* are closely correlated with progression of inflammatory bowel disease and a raised risk of obesity (Gao et al., 2021; Ji et al., 2021), and were also found to be enriched in ALD mice (Liu, Luo, et al., 2020; Xiao et al., 2020). *Bacteroides*, a Gram-negative anaerobe, is an important source of pathogenic factors such as LPS and capsule polysaccharides, and has been recognized as a key indicator for confirming patients with alcohol use disorders (Addolorato et al., 2020). Previous studies have indicated that ALD and intestinal diseases are associated with elevated levels of pro-inflammatory *Parabacteroides* in murine intestines (Liu et al., 2019; Xia et al., 2020). In the current work, *Parabacteroides* presented a tightly positive correlation with proinflammatory factors, LPS levels and liver function indicators, and also a strikingly opposite correlation with intestinal barrier-related proteins (Fig. 10). In line with our results, Xia et al. (2020) reported that *Parabacteroides* displayed an inverse correlation with TJ proteins and also a positive association with hepatic inflammation and oxidative stress parameters. Apparently, the relative abundance of aforementioned typical pathobionts was sharply reduced after HJPS-H administration in comparison to the EtOH group. By contrast, some benign microorganisms were enriched responding to HJPS-H intervention and might mediate the protective effects of HJPS against ALD via promoting SCFAs' production and strengthening intestinal barrier function. *Akkermansia*, a known LPS-suppressive genus, colonizes intestinal mucous layer, where it not only provides nutrition for enterocytes by degrading mucin to produce SCFAs, but also promotes barrier function by enhancing mucus production, thereby preventing inflammation and maintaining the host's metabolic homeostasis (Fan et al., 2019; Grander et al., 2017). Simultaneously, Grander et al. (2017) discovered that the *Akkermansia muciniphila* abundance in feces was indirectly associated with the severity of liver disease, and the restoration of gut *A. muciniphila* depletion through oral *A. muciniphila* supplementation could effectively alleviate EtOH-induced hepatic injury and neutrophil infiltration both prophylactically and therapeutically. Intriguingly, deficiency of *Eubacterium coprostanoligenes group* was

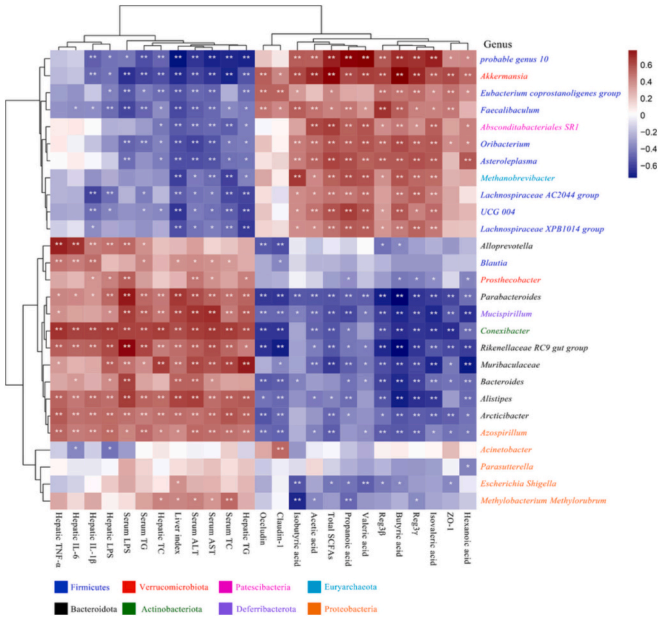

Fig. 10. Heatmap shows spearman's rank correlations between specific gut taxa selected through LEfSe analysis and ALD-related indicators. The color scale reflects the spearman R value, with red and blue representing positive and negative correlations, respectively. $*p < 0.05$ and $**p < 0.01$ according to Spearman's rank correlation coefficient. (For interpretation of the references to color in this figure legend, the reader is referred to the web version of this article.)

commonly found in mice with obesity and colitis (Guo et al., 2022; Yang, Ji, et al., 2020). Studies have reported that *Eubacterium coprostanoligenes group* could not only convert cholesterol into inabsorbable coprosterol to regulate cholesterol metabolism and serum cholesterol levels, but also up-regulate P-glycoprotein expression through participating in BAs conversion and promoting SCFAs' secretion, thereby restraining hyperactive inflammation and preserving intestinal homeostasis (Guo et al., 2022; Yang, Ji, et al., 2020).

On the other hand, PICRUSt analysis suggested that genes in human diseases' pathways were activated, whereas genes associated with metabolic and environment information processing were down-regulated in the EtOH group compared with the Ctrl group, which were apparently reversed after HJPS-H intake (Fig. 7), possibly implying the essentiality of gut microbiota restoration in terms of ALD recovery. A similar finding reported by Zhou et al. (2023) indicated that intestinal flora of polysaccharides UBDP-treated group was increasingly enriched in categories regarding basic metabolic pathways (membrane transport, carbohydrate metabolism, amino acid metabolism and energy metabolism) compared to that of the diabetic rats, highlighting the effective recovery of polysaccharides on gut microbiome dysfunction. Comparing topological features of gut microbial co-occurrence networks among different groups (Fig. 8), it was speculated that the transition of microbial network features from scale-free to stochastic might be accompanied by the progression of ALD pathology. Moreover, compared with the EtOH group, HJPS-H supplementation optimized gut microbiota topology to some extent and maintained a homeostasis of co-occurrence and co-exclusion patterns among microbes, inferring that HJPS-H ingestion might tend to activate specific genera that played pivotal roles in the network and promote their cooperation to correct EtOH-induced flora dysbiosis. Meanwhile, dissimilarities of bacterial co-abundance networks emphasized the potential significance of some relatively low-abundance genera in the overall microbial interaction modes.

Non-digestible carbohydrates can be fermented by colonic microorganisms to produce SCFAs, which are not only significant energy source for intestinal epithelial cells, but also promote acidification of colonic environment and prevent growth of pathogens (Lv, Guo, Li, Yu, & Liu, 2019). It is widely recognized that SCFAs play a vital role as signaling molecules in diverse critical physiological activities of the host through gut-liver axis (Fang et al., 2019; Lv et al., 2019; Sun et al., 2019). Acetic acid, the most abundant SCFA in colon, was reported to reach liver through portal vein circulation and participate in hepatic fatty acid metabolism as a precursor of C16 and C18 fatty acid synthesis (Kindt et al., 2018). Propionic acid was found to be involved in glycogenesis, inhibition of cholesterol synthesis and reduction of hepatic fat deposition (Sun et al., 2019). A growing body of evidence supports pleiotropic benefits of butyric acid, including facilitating proliferation of healthy colon cells, stabilizing intestinal microenvironment, sustaining intestinal mucosal barrier function, modulating the balance of immune and lipid metabolism, antibacterial and anti-inflammatory (Peng, Li, Green, Holzman, & Lin, 2009; Qiao, Qian, Wang, Ma, & Wang, 2014; Ren et al., 2022; Rivera-Chávez et al., 2016). Ren et al. (2022) highlighted the protective effect of butyrate against ALD via regulating Mψ polarization and inhibiting LPS-TLR4-NF-κB/NLRP3 axis through mediating GPR43-ARRB2 signaling pathway. Recent data confirmed that butyrate complementing prevented EtOH-mediated destruction of intestinal TJs and hepatic inflammation (Cresci, Bush, & Nagy, 2014). In the present research, EtOH exposure resulted in a remarkable decline in concentrations of seven SCFAs in colonic contents, which was consistent with previous studies (Fang et al., 2019; Li et al., 2021). Intriguingly, HJPS-H administration markedly elevated four SCFAs' levels and the total SCFAs content in comparison to the EtOH group (Fig. 9), which might be attributed to increment of non-digestible carbohydrates' content in colon and enrichment of intestinal SCFA producers. *Akkermansia* mainly produces propionic acid, while *Eubacterium coprostanoligenes group* is a major producer of butyrate. These genera jeopardized by excessive EtOH consumption were, as expected, enriched in the HJPS-H group (Figs. 6E and S2). Meanwhile, correlation analysis (Fig. 10) clarified that these genera were strongly positively correlated with butyric acid, isobutyric acid, isovaleric acid, hexanoic acid and total SCFAs, whereas intensely negatively associated with liver function indexes and LPS at both liver and circulatory levels. In general, HJPS-H ingestion might increase intestinal SCFAs' levels not only through raising non-digestible carbohydrates' content in colon, but also via impeding overgrowth of pathogenic bacteria and restoring dominant SCFAs-producing bacteria, leading to enhanced intrinsic defense of intestinal mucosa, prevented LPS dissemination and suppressed hepatic inflammatory cascade reaction, thus ameliorating ALD.

5. Conclusions

Structural elucidation of purified HJPS1–2 (Mw of 3.49 kDa) suggested that it consisted of a → 4)-α-D-Glcp-(1 → backbone and the side chain was α-D-Glcp-(1 → 6)-α-D-Glcp-(1 → linked at C6-position of → 4,6)-α-D-Glcp-(1 →. The favorable effect of HJPS1–2 against ALD was further confirmed as evidenced by the improvement of serum and liver biochemical parameters and the reduction of aberrant hepatic lipid accumulation. Besides, the upregulated expressions of ZO-1, occludin, claudin-1, Reg3β and Reg3γ, combined with corrected gut microbial community disorder in HJPS-treated mice relative to EtOH group implied enhancement of intestinal barrier integrity and gut ecology, which might be responsible for the decrease of circulating LPS level and hepatic inflammation. Furthermore, HJPS1–2 supplementation might elevate colonic SCFAs' contents through raising non-digestible carbohydrates' content and modulating specific gut taxa, thereby indirectly mediating the ALD amelioration. The beneficial outcomes of HJPS1–2 in our study support the potential of dietary strategies to mitigate ALD in the early stage and provide a theoretical basis for further attenuating health risks of traditional fermented wine.

Funding

This research was funded by the National Key Research and Development Program of China (No. 2022YFD2101204) and the National Natural Science Foundation of China (32202025, 22138004 and 32001828).

CRediT authorship contribution statement

Yi Yang: Methodology, Formal analysis, Investigation, Writing – original draft, Writing – review & editing, Visualization. **Qingxi Ren:** Methodology, Supervision, Writing – review & editing, Project administration. **Zhilei Zhou:** Conceptualization, Resources, Project administration. **Xiong Li:** Validation, Formal analysis, Investigation. **Dongliang Ren:** Formal analysis, Visualization. **Zhongwei Ji:** Resources, Methodology. **Jian Mao:** Conceptualization, Resources, Supervision, Funding acquisition.

Declaration of competing interest

The authors declare that they have no known competing financial interests or personal relationships that could have appeared to influence the work reported in this paper.

Data availability

Data will be made available on request.

Appendix A. Supplementary data

Supplementary data to this article can be found online at https://doi.org/10.1016/j.carbpol.2023.121423.

References

Addolorato, G., Ponziani, F. R., Dionisi, T., Mosoni, C., Vassallo, G. A., Sestito, L., et al. (2020). Gut microbiota compositional and functional fingerprint in patients with alcohol use disorder and alcohol-associated liver disease. *Liver International, 40*(4), 878–888.

Agrawal, P. K. (1992). NMR spectroscopy in the structural elucidation of oligosaccharides and glycosides. *Phytochemistry, 31*(10), 3307–3330.

Bertola, A., Mathews, S., Ki, S. H., Wang, H., & Gao, B. (2013). Mouse model of chronic and binge ethanol feeding (the NIAAA model). *Nature Protocols, 8*(3), 627–637.

Bhat, A. A., Uppada, S., Achkar, I. W., Hashem, S., Yadav, S. K., Shanmugakonar, M., et al. (2019). Tight junction proteins and signaling pathways in cancer and inflammation: A functional crosstalk. *Frontiers in Physiology, 9*, 1942.

Björndal, H., Lindberg, B., & Svensson, S. (1967). Mass spectrometry of partially methylated alditol acetates. *Carbohydrate Research, 5*(4), 433–440.

Cai, L. L., Zou, S. S., Liang, D. P., & Luan, L. B. (2018). Structural characterization, antioxidant and hepatoprotective activities of polysaccharides from *Sophorae tonkinensis Radix*. *Carbohydrate Polymers, 184*, 354–365.

Cao, J. J., Lv, Q. Q., Zhang, B., & Chen, H. Q. (2019). Structural characterization and hepatoprotective activities of polysaccharides from the leaves of *Toona sinensis* (A. Juss) Roem. *Carbohydrate Polymers, 212*, 89–101.

Chen, G. M., Huang, Z. R., Wu, L., Wu, Q., Guo, W. L., Zhao, W. H., et al. (2021). Microbial diversity and flavor of Chinese rice wine (*Huangjiu*): An overview of currentresearch and future prospects. *Current Opinion in Food Science, 42*, 37–50.

Cresci, G. A., Bush, K., & Nagy, L. E. (2014). Tributyrin supplementation protects mice from acute ethanol-induced gut injury. *Alcoholism, Clinical and Experimental Research, 38*(6), 1489–1501.

Fan, J. J., Wang, Y. S., You, Y., Ai, Z. Y., Dai, W. C., Piao, C. H., et al. (2019). Fermented ginseng improved alcohol liver injury in association with changes in the gut microbiota of mice. *Food & Function, 10*(9), 5566–5573.

Fang, C., Du, H., Zheng, X. J., Zhao, A. H., Jia, W., & Xu, Y. (2019). Solid-state fermented Chinese alcoholic beverage (*Baijiu*) and ethanol resulted in distinct metabolic and microbiome responses. *The FASEB Journal, 33*(6), 7274–7288.

Gao, J., Mao, K., Wang, X. H., Mi, S., Fu, M. Q., Li, X. Y., et al. (2021). Tibet kefir milk regulated metabolic changes induced by high-fat diet via amino acids, bile acids, and equol metabolism in human-microbiota-associated rats. *Journal of Agricultural and Food Chemistry, 69*(23), 6720–6732.

Grander, C., Adolph, T. E., Wieser, V., Lowe, P., Wrzosek, L., Gyongyosi, B., et al. (2017). Recovery of ethanol-induced *Akkermansia muciniphila* depletion ameliorates alcoholic liver disease. *Gut, 67*(5), 892.

Guarner, F., & Malagelada, J. R. (2003). Gut flora in health and disease. *The Lancet, 361*(9356), 512–519.

Guo, T. T., Yang, Y., Gao, M. J., Qu, Y., Guo, X. X., Liu, Y., et al. (2020). *Lepidium meyenii* Walpers polysaccharide and its cationic derivative re-educate tumor-associated macrophages for synergistic tumor immunotherapy. *Carbohydrate Polymers, 250*(15), 116904.

Guo, W. J., Mao, B. Y., Cui, S. M., Tang, X., Zhang, Q. X., Zhao, J. X., et al. (2022). Protective effects of a novel probiotic *Bifidobacterium pseudolongum* on the intestinal barrier of colitis mice via modulating the PPARγ/STAT3 pathway and intestinal microbiota. *Foods, 11*(11), 1551.

Huang, J. F., Ou, Y. X., Yew, T. W. D., Liu, J. N., Leng, B., Lin, Z. H., et al. (2016). Hepatoprotective effects of polysaccharide isolated from *Agaricus bisporus* industrial wastewater against CCl_4-induced hepatic injury in mice. *International Journal of Biological Macromolecules, 82*, 678–686.

Huo, J. Y., Liao, Q. J., Wu, J. H., Zhao, D., Sun, W. Z., An, M. Z., et al. (2022). Structure elucidation and intestinal barrier protection of an α-D-glucan in *Huangshui*. *International Journal of Biological Macromolecules, 223*, 595–605.

Ji, M., Fang, C., Jia, W., Du, H., & Xu, Y. (2021). Regulatory effect of volatile compounds in fermented alcoholic beverages on gut microbiota and serum metabolism in mouse model. *Food & Function, 12*(12), 5576–5590.

Jiang, Y., Shang, Z. P., Lv, X. Y., Du, M., Ma, L., Hou, G. G., et al. (2022). Structure elucidation and antitumor activity of a water soluble polysaccharide from *Hemicentrotus pulcherrimus*. *Carbohydrate Polymers, 292*, 119718.

Kim, H., Lee, H., & Shin, K. S. (2016). Intestinal immunostimulatory activity of neutral polysaccharide isolated from traditionally fermented Korean brown rice vinegar. *Bioscience, Biotechnology, and Biochemistry, 80*(12), 2383–2390.

Kindt, A., Liebisch, G., Clavel, T., Haller, D., Hörmannsperger, G., Yoon, H., et al. (2018). The gut microbiota promotes hepatic fatty acid desaturation and elongation in mice. *Nature Communications, 9*(1), 3760.

Li, H. Y., Cao, W. X., Xie, J. W., Che, H. X., Liu, L., Dong, X. F., et al. (2022). α-D-1,6-glucan from *Castanea mollissima* Blume alleviates dextran sulfate sodium-induced colitis *in vivo*. *Carbohydrate Polymers, 289*, 119410.

Li, H. Z., Shi, J. L., Zhao, L., Guan, J. Q., Liu, F., Huo, G. C., et al. (2021). *Lactobacillus plantarum* KLDS1.0344 and *Lactobacillus acidophilus* KLDS1.0901 mixture prevents chronic alcoholic liver injury in mice by protecting the intestinal barrier and regulating gut microbiota and liver-related pathways. *Journal of Agricultural and Food Chemistry, 69*(1), 183–197.

Li, P., Xiao, N., Zeng, L. P., Xiao, J., Huang, J. Z., Xu, Y. N., et al. (2020). Structural characteristics of a mannoglucan isolated from Chinese yam and its treatment effects against gut microbiota dysbiosis and DSS-induced colitis in mice. *Carbohydrate Polymers, 250*, 116958.

Liu, W., Tang, S., Zhao, Q. Q., Zhang, W. Y., Li, K. D., Yao, W. B., et al. (2020). The α-D-glucan from marine fungus *Phoma herbarum* YS4108 ameliorated mice colitis by repairing mucosal barrier and maintaining intestinal homeostasis. *International Journal of Biological Macromolecules, 149*, 1180–1188.

Liu, X. X., Zhao, K., Yang, X. B., & Zhao, Y. (2019). Gut microbiota and metabolome response of *Decaisnea insignis* seed oil on metabolism disorder induced by excess alcohol consumption. *Journal of Agricultural and Food Chemistry, 67*(38), 10667–10677.

Liu, Y., Luo, Y. K., Wang, X. H., Luo, L. Y., Sun, K., & Zeng, L. (2020). Gut microbiome and metabolome response of pu-erh tea on metabolism disorder induced by chronic alcohol consumption. *Journal of Agricultural and Food Chemistry, 68*(24), 6615–6627.

Liu, Y. Q., Yin, F., Huang, L. S., Teng, H. F., Shen, T. Y., & Qin, H. L. (2021). Long-term and continuous administration of *Bacillus subtilis* during remission effectively maintains the remission of inflammatory bowel disease by protecting intestinal integrity, regulating epithelial proliferation, and reshaping microbial structure and function. *Food & Function, 12*(5), 2201–2210.

Luo, Y. Y., Li, C. L., He, T. S., Huang, W. J., Wang, Y. R., Yu, D. B., et al. (2022). A highly branched α-d-glucan facilitates antitumor immunity by reducing cancer cell CXCL5 expression. *International Journal of Biological Macromolecules, 209*, 166–179.

Lv, X. C., Guo, W. L., Li, L., Yu, X. D., & Liu, B. (2019). Polysaccharide peptides from *Ganoderma lucidum* ameliorate lipid metabolic disorders and gut microbiota dysbiosis in high-fat diet-fed rats. *Journal of Functional Foods, 57*, 48–58.

Ma, Z. Y., Sun, Q. Y., Chang, L. L., Peng, J., Zhang, M. Q., Ding, X. C., et al. (2022). A natural anti-obesity reagent derived from sea buckthorn polysaccharides: Structure characterization and anti-obesity evaluation *in vivo*. *Food Chemistry, 375*, 131884.

Peng, L., Liu, S. P., Ji, Z. W., Chen, S. G., & Mao, J. (2019). Structure characterisation of polysaccharide isolated from huangjiu and its anti-inflammatory activity through MAPK signalling. *International Journal of Food Science & Technology, 54*(5), 1874–1883.

Peng, L. Y., Li, Z. R., Green, R. S., Holzman, I. R., & Lin, J. (2009). Butyrate enhances the intestinal barrier by facilitating tight junction assembly via activation of AMP-activated protein kinase in Caco-2 cell monolayers. *The Journal of Nutrition, 139*(9), 1619–1625.

Qiao, Y. L., Qian, J. M., Wang, F. R., Ma, Z. Y., & Wang, Q. W. (2014). Butyrate protects liver against ischemia reperfusion injury by inhibiting nuclear factor kappa B activation in Kupffer cells. *Journal of Surgical Research, 187*(2), 653–659.

Ren, Y., Wang, R., Yu, J. J., Bao, T., Liu, Y. J., Bai, Z. X., et al. (2022). Butyrate ameliorates inflammation of alcoholic liver disease by suppressing the LPS-TLR4-NF-κB/NLRP3 axis via binding GPR43-β-arrestin2. *Journal of Functional Foods, 99*, 105351.

Rivera-Chávez, F., Zhang, L. F., Faber, F., Lopez, C. A., Byndloss, M. X., Olsan, E. E., et al. (2016). Depletion of butyrate-producing *Clostridia* from the gut microbiota drives an aerobic luminal expansion of *Salmonella*. *Cell Host & Microbe, 19*(4), 443–454.

Sarin, S. K., Pande, A., & Schnabl, B. (2019). Microbiome as a therapeutic target in alcohol-related liver disease. *Journal of Hepatology, 70*(2), 260–272.

Sassaki, G. L., Gorin, P. A. J., Souza, L. M., Czelusniak, P. A., & Iacomini, M. (2005). Rapid synthesis of partially O-methylated alditol acetate standards for GC-MS: Some relative activities of hydroxyl groups of methyl glycopyranosides on purdie methylation. *Carbohydrate Research, 340*, 731–739.

Shen, C., Mao, J., Chen, Y. Q., Meng, X. Y., & Ji, Z. W. (2015). Extraction optimization of polysaccharides from Chinese rice wine from the Shaoxing region and evaluation of its immunity activities. *Journal of the Science of Food and Agriculture, 95*(10), 1991–1996.

Silveira, M. L. L., Smiderle, F. R., Moraes, C. P., Borato, D. G., Baggio, C. H., Ruthes, A. C., et al. (2014). Structural characterization and anti-inflammatory activity of a linear β-D-glucan isolated from *Pleurotus sajor-caju. Carbohydrate Polymers, 113*, 588–596.

Son, S. U., Kim, H. W., Park, M. S., & Shin, K. S. (2022). Effects of intravenous administration of polysaccharide purified from fermented barley on tumor metastasis inhibition *via* immunostimulating activities. *Food Bioscience, 49*, 101833.

Sun, Y. J., Cui, X. Y., Duan, M. M., Ai, C. Q., Song, S., & Chen, X. F. (2019). *In vitro* fermentation of κ-carrageenan oligosaccharides by human gut microbiota and its inflammatory effect on HT29 cells. *Journal of Functional Foods, 59*, 80–91.

Takaya, Y., Uchisawa, H., Ichinohe, H., Sasaki, J. I., Ishida, K., & Matsue, H. (1998). Antitumor glycogen from scallops and the interrelationship of structure and antitumor activity. *Journal of Marine Biotechnology, 6*(4), 208–213.

Teng, S. S., Zhang, Y. F., Jin, X. H., Zhu, Y. F., Li, L. Z., Huang, X. W., et al. (2023). Structure and hepatoprotective activity of Usp10/NF-κB/Nrf2 pathway-related *Morchella esculenta* polysaccharide. *Carbohydrate Polymers, 303*, 120453.

Wang, J., Zhang, B., Wu, Q., Jiang, X. Y., Liu, H. J., Wang, C. Z., et al. (2022). Sensomics-assisted flavor decoding of coarse cereal Huangjiu. *Food Chemistry, 381*, 132296.

Wang, N. N., Xu, P. C., Yao, W. X., Zhang, J. L., Liu, S. F., Wang, Y. J., et al. (2021). Structural elucidation and anti-diabetic osteoporotic activity of an arabinogalactan from *Phellodendron chinense* Schneid. *Carbohydrate Polymers, 271*, 118438.

Wang, Q. C., Wei, M. S., Yue, Y., Wu, N., Wang, J., & Zhang, Q. B. (2021). Structural characterization and immunostimulatory activity *in vitro* of a glycogen from sea urchin-*Strongylocentyotus internedius*. *Carbohydrate Polymers, 258*, 117701.

Wei, W., Feng, L., Bao, W. R., Ma, D. L., Leung, C. H., Nie, S. P., et al. (2016). Structure characterization and immunomodulating effects of polysaccharides isolated from *Dendrobium officinale*. *Journal of Agricultural and Food Chemistry, 64*(4), 881–889.

Wu, J. X., Shao, H. R., Zhang, J. H., Ying, Y., Cheng, Y. L., Zhao, D., et al. (2019). Mussel polysaccharide α-D-glucan (MP-A) protects against non-alcoholic fatty liver disease via maintaining the homeostasis of gut microbiota and regulating related gut-liver axis signaling pathways. *International Journal of Biological Macromolecules, 130*, 68–78.

Wu, Y. B., Liu, C., Jiang, Y. Q., Bai, B. K., He, X. H., Wang, H. R., et al. (2022). Structural characterization and hepatoprotective effects of polysaccharides from *Anoectochilus zhejiangensis*. *International Journal of Biological Macromolecules, 198*, 111–118.

Wu, Y. L., Zhou, F., Jiang, H. T., Wang, Z. J., Hua, C., & Zhang, Y. S. (2018). Chicory (*Cichorium intybus* L.) polysaccharides attenuate high-fat diet induced non-alcoholic fatty liver disease via AMPK activation. *International Journal of Biological Macromolecules, 118*, 886–895.

Xia, T., Zhang, B., Li, S. P., Fang, B., Duan, W. H., Zhang, J., et al. (2020). Vinegar extract ameliorates alcohol-induced liver damage associated with the modulation of gut microbiota in mice. *Food & Function, 11*(4), 2898–2909.

Xiao, J., Wu, C. J. H., He, Y. G., Guo, M. Y., Peng, Z. T., Liu, Y. X., et al. (2020). Rice bran phenolic extract confers protective effects against alcoholic liver disease in mice by alleviating mitochondrial dysfunction via the PGC-1α-TFAM pathway mediated by microRNA-494-3p. *Journal of Agricultural and Food Chemistry, 68*(44), 12284–12294.

Xie, X., Shen, W., Zhou, Y. R., Ma, L. M., Xu, D. Y., Ding, J. L., et al. (2020). Characterization of a polysaccharide from *Eupolyphaga sinensis* walker and its effective antitumor activity via lymphocyte activation. *International Journal of Biological Macromolecules, 162*, 31–42.

Xu, H. L., Guo, T. T., Guo, Y. F., Zhang, J. P., Li, Y., Feng, W. H., et al. (2007). Characterization and protection on acute liver injury of a polysaccharide MP-I from *Mytilus coruscus. Glycobiology, 18*(1), 97–103.

Yang, H., Hua, J. L., & Wang, C. (2019). Anti-oxidation and anti-aging activity of polysaccharide from *Malus micromalus Makino* fruit wine. *International Journal of Biological Macromolecules, 121*, 1203–1212.

Yang, X. B., Mo, W. J., Zheng, C. J., Li, W. Z., Tang, J., & Wu, X. Y. (2020). Alleviating effects of noni fruit polysaccharide on hepatic oxidative stress and inflammation in rats under a high-fat diet and its possible mechanisms. *Food & Function, 11*(4), 2953–2968.

Yang, X. Q., Wu, Y. H., Zhang, C., Fu, S., Zhang, J. M., & Fu, C. M. (2020). Extraction, structural characterization, and immunoregulatory effect of a polysaccharide fraction from Radix Aconiti Lateralis Preparata (Fuzi). *International Journal of Biological Macromolecules, 143*(15), 314–324.

Yang, Y., Ji, J., Di, L. Q., Li, J. S., Hu, L. H., Qiao, H. Z., et al. (2020). Resource, chemical structure and activity of natural polysaccharides against alcoholic liver damages. *Carbohydrate Polymers, 241*, 116355.

Yang, Y., Zhou, Z. L., Liu, Y. F., Xu, X. B., Xu, Y. Z., Zhou, W. B., et al. (2022). Non-alcoholic components in Huangjiu as potential factors regulating the intestinal barrier and gut microbiota in mouse model of alcoholic liver injury. *Foods, 11*(11), 1537.

Ye, Y. T., Wang, L. X., Zhan, P., Tian, H. L., & Liu, J. S. (2022). Characterization of the aroma compounds of Millet Huangjiu at different fermentation stages. *Food Chemistry, 366*, 130691.

Ying, M. X., Yu, Q., Zheng, B., Wang, H., Wang, J. H., Chen, S. P., et al. (2020). Cultured *Cordyceps sinensis* polysaccharides modulate intestinal mucosal immunity and gut microbiota in cyclophosphamide-treated mice. *Carbohydrate Polymers, 235*, 115957.

Yuan, Q. X., Zhang, J., Xiao, C. L., Harqin, C., Ma, M. Y., Long, T., et al. (2020). Structural characterization of a low-molecular-weight polysaccharide from *Angelica pubescens* Maxim. f. *biserrata* Shan et Yuan root and evaluation of its antioxidant activity. *Carbohydrate Polymers, 236*, 116047.

Zhang, J. J., Liu, M., Yang, Y. S., Lin, L., Xu, N., Zhao, H. J., et al. (2016). Purification, characterization and hepatoprotective activities of mycelia zinc polysaccharides by *Pleurotus djamor*. *Carbohydrate Polymers, 136*, 588–597.

Zhang, S. J., Zhang, H., Shi, L. J., Li, Y., Tuerhong, M., Abudukeremu, M., et al. (2021). Structure features, selenylation modification, and improved anti-tumor activity of a polysaccharide from *Eriobotrya japonica. Carbohydrate Polymers, 273*, 118496.

Zhang, Z. H., Fan, S. T., Huang, D. F., Yu, Q., Liu, X. Z., Li, C., et al. (2018). Effect of *lactobacillus plantarum* NCU116 fermentation on *Asparagus officinalis* polysaccharide: Characterization, antioxidative, and immunoregulatory activities. *Journal of Agricultural and Food Chemistry, 66*(41), 10703–10711.

Zhao, B. T., Wu, J. B., Li, J. H., Bai, Y., Luo, Y., Ji, B., et al. (2020). Lycopene alleviates DSS-induced colitis and behavioral disorders via mediating microbes-gut-brain axis balance. *Journal of Agricultural and Food Chemistry, 68*(13), 3963–3975.

Zhou, W., Han, L. J., Raza, S. H. A., Yue, Q. M., Sun, S. N., Zhao, Y. X., et al. (2023). Polysaccharides in *Berberis dasystachya* improve intestinal flora depending on the molecular weight and ameliorate type 2 diabetes in rats. *Journal of Functional Foods, 100*, 105381.